Applied Biochemistry and Biotechnology (2024) 196:841–877
https://doi.org/10.1007/s12010-023-04547-1

ORIGINAL ARTICLE

Therapeutic Potential of HMF and Its Derivatives: a Computational Study

Shashank Kumar Singh[1] · Soumya Sasmal[2] · Yatender Kumar[1]

Accepted: 12 April 2023 / Published online: 24 May 2023

Abstract
Over the past century, chemicals and energy have increasingly been derived from non-renewable resources. The growing demand for essential chemicals and shrinking inventory make reliable, sustainable sources essential. Carbohydrates offer by far the greatest carbon supply. Furan compounds, a particular family of dehydration products, are believed to offer high chemical potential. Here, we analyze 5-HMF (5, hydroxymethylfurfural) and some of its derivatives in particular, a furan-type platform chemical. To analyze the therapeutic potential of HMF and its derivatives, this study utilized cutting-edge technologies such as computer-aided drug design, virtual screening, molecular docking, and molecular dynamic simulation. We conducted 189 docking simulations and examined some of the most promising dock poses using the molecular dynamic simulator. As for the receptors for our compounds, the leading candidates are human acetylcholinesterase, beta-lactamases, *P. aeruginosa* LasR, and *S. aureus* tyrosyl-tRNA synthetases. Out of all derivatives considered in this study, 2,5-furandicarboxylic acid (FCA) performed best.

Keywords HMF · Docking · MD Simulation · Therapeutic · Antimicrobial

Introduction

Chemicals and energy have become increasingly dependent on non-renewable resources over the past century. According to projections, the demand for chemicals will see a massive increase in the coming years due to strong economic and demographic growth. Developing new, sustainable sources of essential chemicals will be crucial due to the growing demand and shrinking inventory. There is particular promise in carbohydrates, which offer by far the greatest natural supply of carbon. In their molecular structures, carbohydrates have an excess of oxygen that hinders their use as feedstock. Dehydration of carbohydrates into rare compounds such as furans is an example of an effective removal strategy [1]. One

✉ Yatender Kumar
yatender.kumar@nsut.ac.in

1 Department of Biological Sciences and Engineering (BSE), Netaji Subhas University of Technology, Dwarka Sector-3, New Delhi 110078, India

2 Department of Biotechnology, Visva Bharati, Santiniketan, West Bengal 731235, India

particular family of dehydration products, furan compounds, is thought to offer a particularly high potential for chemical manufacturing.

In this study, we focus on one particular furan-type platform chemical, 5-HMF (5, hydroxymethylfurfural) in particular. Numerous monomeric compounds can be produced from 5-HMF, a platform molecule. It contains hydroxymethyl and formyl substituents at positions 2 and 5, respectively, both of which are capable of oxidation. It is challenging to carry out either the former or the latter's selective oxidation without influencing the other. Various industrial applications are available for each of the oxidation products, including fine chemicals, intermediates, and monomers. The choice of catalyst, oxidant, and reaction phase is critical in these conversion reactions [2]. Fresh meals rarely contain HMF, but foods with sugar often do when they are preserved, particularly when they are dried or heated. The causal component in honey affects the pharmacokinetics and pre-systemic metabolism of glycyrrhizin (GZ) in vivo. HMF acts as an indication and a Maillard reaction product in meals [3].

In 5-HMF production, the glucose from biomass carbohydrates needs to be transformed to fructose before being converted to 5-HMF [4]. The cellulose in the biomass must be exposed to the acid hydrolysis reaction in order for it to be converted into hexose sugar, which calls for pretreatment of the biomass to remove lignin and possibly hemicellulose. The hemicellulose of biomass is where pentoses like xylose, which can be converted into furfural by acid hydrolysis, are found in biomass carbohydrates [5]. Meanwhile, research on the conversion of pretreated biomass to 5-HMF via acid hydrolysis of C6 sugar has been sparse. Typically, the ionic liquid is a key factor in the catalytic conversion of biomass to 5-HMF. In order to create 5-HMF, an ionic liquid has been employed as a reaction medium with an acid catalyst. Rice straw and wood that had been pretreated with acids and bases had a high output of 5-HMF when it was hydrolyzed in [BMIM]Cl under the influence of $CrCl_3$ $6H_2O$ [6]. The HMF can subsequently be transformed into a wide range of products, including polymer monomers, fine chemicals, fuel additives, liquid fuels, and other platform chemicals with a wide spectrum of structural complexity, which can be used for a variety of applications [7].

2,5-Furandicarboxylic acid (FCA) is a promising bio-based aromatic monomer that can be utilized to produce novel bio-based polymeric materials. There are several approaches to manufacture FCA, including the 5-hydroxymethylfurfural (HMF) route, the hexose acid route, the furfural route, and the diglycol acid method. The HMF route stands out among them as being the most significant and promising one for the commercialization of FCA [8]. The anticancer effect [9], the pharmaceutical preparation of benzylamine moieties, and the renewable building block status of 2,5-furan-dimethanol make it a well-known chemical in the pharmaceutical industry [10]. Furthermore, by using hydrogen or a hydrogen donor and removing the oxygen as water, hydrogenation or hydrogenolysis can convert furfural and HMF into MF and DMF [11]. 2,5-Dimethylfuran (DMF) belongs to the category of furans in which the hydrogen atoms at positions 2 and 5 are swapped out for methyl groups. It functions as a metabolite in human urine, an antifungal, a bacterium, a fumigant, a fuel, a metabolite in plants, and a Maillard reaction product [12]. Furan-2,5-dicarbaldehyde, also known as 2,5-diformylfuran, belongs to the group of furans and has two formyl substituents at positions 2 and 5. It is an arene carbaldehyde and a dialdehyde that belongs to the furan family. For the manufacture of drugs, fungicides, furan-urea resins, or heterocyclic ligands, it is a flexible chemical intermediate produced as a result of the oxidation of 5-HMF [13].

Modern drug development initiatives often start with basic research before advancing gradually to a series of precise tasks that, if successful, lead to the creation of a novel

medicine for the treatment of human disease and other diseases. It is evident that nature has played a significant part in this process and will continue to do so. The imperative need for new medicines for the treatment of cancer, HIV, and other infectious diseases, as well as a variety of other diseases and disorders, mandates a comprehensive examination of all drug discovery strategies [14]. Investigation of lead compounds from a renewable bio-based source is a particularly profitable area of study in this direction. HMF and its derivatives can be used for its potential as a therapeutic lead compound because of its fantastic industrial applications. The process of finding new drugs in pharmaceutical research takes a long time. Clinical trials are usually completed in 10 to 14 years. The likelihood of a new chemical making it to a clinical trial is quite low. Additionally, billions must be invested. Modern biomedical engineering techniques are the solution to these issues. The increased availability of chemical compound libraries and automatic screening techniques has made it relatively simple and easy to identify first lead candidates for new therapeutic targets [15]. The objective of this study is to utilize cutting-edge technologies, such as computer-aided drug design, virtual screening, molecular docking, and molecular dynamic simulation, to concentrate on analyzing the therapeutic potential of HMF and its derivatives. These contemporary technologies, such as drug dosage form optimization and drug delivery system development, are particularly helpful for pharmaceutical research. The present development of docking-based virtual screening results in the identification of a new target molecule, which is then designed using computer-aided drug design. Manufacturing or dose modification may ultimately result in some promising lead compounds. An overview of the study is illustrated in the Graphical Abstract.

Material and Methods

Identification and Collection of Receptors and Ligands

Out of several derivatives, as identified in the literature survey, some non-conventional derivatives are identified and are taken up in this study, listed in Table 1. All the relevant information and SMILES were collected from PubChem, a database maintained by the National Center for Biotechnology Information (NCBI). Structures of all the ligands were also downloaded as SDF files from PubChem. Similarly, with the help of a thorough literature survey, several important receptors/enzymes in humans and microorganisms are identified to test the potential of selected ligands as mentioned above. All receptors/enzymes' three-dimensional structures were retrieved from the Protein Data Bank.

Pre-processing of Data

The Computer-Aided Drug Design (CADD) Group of the Chemical Biology Laboratory (CBL), NCI, NIH, located at the Frederick National Laboratory for Cancer Research (FNLCR), USA, converts all ligands data collected from as SDF files to 3D structures with PDB files using the CADD Group's Chemoinformatics Tools and User Services. Additionally, all of the PDB structures are cross-checked with PubChem structures to ensure that there were no conversion artifacts. With the aid of information from the RCSB Protein Data Bank, all protein structures were examined for resolution and any noteworthy mutation. The binding site of a natural substrate, literature, and the active site prediction tool of BIOVIA Discovery Studio was used to identify the active site of each target protein.

ADMET Study

The pkCSM ADMET descriptors algorithm approach was used to identify PK (pharmacokinetic) features of pharmaceuticals, for instance absorption, distribution, metabolism, excretion, and toxicity (ADMET) profiling. Lipophilicity levels expressed as atom-based LogP and 2D polar surface area (PSA 2D) are two critical chemical characteristics that significantly influence fractional absorption (AlogP98). These two chemical descriptors have a strong relationship with PK characteristics. Skin permeability, intestinal absorption, intestinal absorption, and P-glycoprotein substrate or inhibitor are a few factors that affect how well medication is absorbed (as shown by the colon cancer cell line [Caco-2]). Medication distribution is influenced by the blood–brain barrier (logBB), CNS permeability, and drug volume of distribution (VDss). To assess metabolism, CYP models for substrate or inhibitor metabolism are utilized (CYP2D6, CYP3A4, CYP1A2, CYP2C19, CYP2C9, CYP2D6, and CYP3A4). To predict excretion, the total clearance model and renal OCT2 substrate are also used. Drug toxicity is predicted by AMES toxicity, hERG inhibition, hepatotoxicity, and cutaneous sensitivity. These variables were calculated, and their limits were checked to ensure they were kept within the projected ranges [16].

Preparation for Docking

The graphical user interface tool AutoDock Tools (ADT) was used to complete intermediary stages such as PDBQT files for protein and ligand preparation and grid box generation. ADT deleted all water molecules and non-standard residues from the protein and assigned it polar hydrogens, united atom Kollman charges, and solvation parameters. The prepared file was saved in PDBQT format by AutoDock tools. Similarly, structures of all the ligand compounds are prepared for docking using AutoDock tools. Polar hydrogen atoms were assigned, all non-polar hydrogen was merged, Gasteiger charges are applied and bond rotations are checked, and then the structure was saved as PDBQT.

Docking with AutoDock Vina

AutoDock Vina was used for docking, and it employed protein and ligand information as well as grid box parameters from the configuration file [17]. Iterated local search global optimizer is used by AutoDock Vina. During the docking process, both the protein and the ligands are treated as stiff. The results with the lowest free energy of binding with positional root mean square deviations (RMSD) of < 1.0 were extracted and aligned with the receptor structure for future investigation.

Molecular Dynamic Simulation

Molecular dynamic modeling was used to investigate the binding stability, conformation, and interaction processes of the selected bioactive compounds (ligands) and receptors. GROMACS 2019.2 [18–20] software was used to perform molecular dynamics

Table 1 Details of compounds used (name, PubChem CID, canonical SMILES, and structure)

S.No.	Name	PubChem CID	Canonical SMILES	Structure
1.	5-Hydroxymethylfurfural (HMF)	237332	C1=C(OC(=C1)C=O)CO	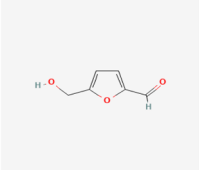
2.	2,5-Furandicarboxylic acid (FCA)	76720	C1=C(OC(=C1)C(=O)O)C(=O)O	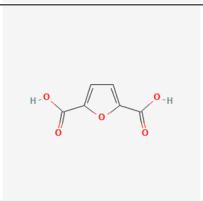
3.	2,5-Bis(hydroxymethyl)furan (BHMF)	74663	C1=C(OC(=C1)CO)CO	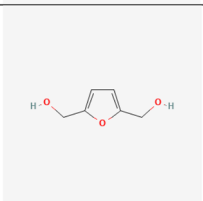
4.	2,5-Dimethylfuran (DMF)	12266	CC1=CC=C(O1)C	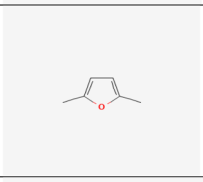
5.	5-(Ethoxymethyl)furan-2-carbaldehyde (EMF)	12648080	CCOCC1=CC=C(O1)C=O	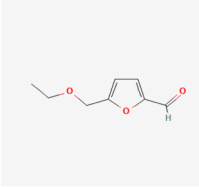
6.	Ethyl levulinate (EL)	10883	CCOC(=O)CCC(=O)C	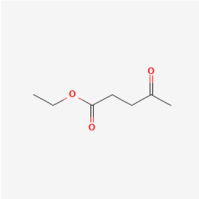
7.	Furan-2,5-dicarbaldehyde (FDC)	69980	C1=C(OC(=C1)C=O)C=O	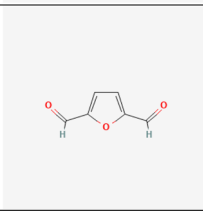

experiments on the selected ligand-receptor complex files. The PRODRG server was used to retrieve the ligands topology [21]. The initial vacuum was minimized for 5000 steps in molecular dynamic simulation using the steepest descent approach. The complex structure in a triclinic box was solved using a simple point charge (SPC) water model. By introducing a sufficient amount of Na + and Cl counterions, the complex system was held at an acceptable salt concentration of 0.15 M. Each complex was given a simulation time of 100 ns from the NPT (isothermal-isobaric, constant number of particles, pressure, and temperature) equilibration for the final run. The GROMACS simulation programme (via the internet server "WebGRO for Macromolecular Simulations (https://simlab.uams.edu/)") was used to perform the root mean square deviation (RMSD) and root mean square fluctuation (RMSF) trajectory analyses.

Results

ADMET Profile

The analysis of ADMET predictions of all the compounds (Table 1) was done using the pkCSM method. The adsorption, distribution, metabolism, excretion, and toxicity profile of test compounds are presented in Table 2. All test compounds are well soluble and absorbed in the intestine, except for DMF, which is recognized as a p-glycoprotein substrate, and FCA, which has a low Caco2 permeability. BHMF and DMF have low VDss in their distribution. All compounds are neither CYP substrates nor inhibitors in terms of metabolism. The excretion of all chemicals seems to be normal. The toxicity profile showed that DMF, EMF, and EL are skin sensitive, but BHMF has a low maximum tolerated dose, whereas EMF was found to be hepatotoxic also.

Docking Study

The HMF and some of its derivatives' (Table 1) binding affinities and modes were projected by the current investigation, as potential targeted ligand molecules against Alzheimer's disease, microbial infection, viral infection, and fungal infection. Table 3 displays the predicted binding affinity of each compound with protein targets.

Alzheimer Targets

Some common protein targets against Alzheimer's disease like human butyrylcholinesterase (BuChE) (PDB ID:4BDS), apolipoprotein E4 (PDB ID:6NCN), β-secretase (PDB ID:4IVT), and human acetylcholinesterase (AChE) (PDB ID:4BDT) were taken and HMF with its derivatives were docked with them. For all four enzyme targets, the docking energy values for the ligands were determined to be in the range of − 3.8 to − 6.2 kcal/mol. The individual lower and upper bounds of binding affinity with all the investigated ligands were − 4.7 to − 6.1, − 3.8 to − 4.8, − 4.2 to 5.2, and − 5.2 to − 6.2 kcal/mol, for 4BDS, 6NCN, 4IVT, and 4BDT, respectively (Table 3). Out of all protein targets, human butyrylcholinesterase and human acetylcholinesterase showed a favorable reception of HMF and its derivatives. HMF bonded with a binding affinity of − 5.3 kcal/mol, EMF bonded with a binding affinity of − 5.6 kcal/mol, and FCA bonded with a binding affinity above − 6 kcal/mol. For BuChE (4BDS) residues, GLY116, GLY117, TYR128, GLU197,

SER198, ALA199, GLU197, and TRP231 most predominantly participated in hydrogen bond formation, whereas residues GLU197, TRP82, HIS438, and TRP231 were involved in hydrophobic interactions (Table 4). BuChE (4BDS) interacted positively with FCA, generating two hydrogen bonds with GLY116 and GLY117; hydrophobic contacts with TRP82 and GLU198; and van der Waals interactions with TRP112, GLY115, TYR128, SER198, ALA199, PHE329, and PHE398 (Table 4). AChE (4BDT) residues THR83, TRP86, TRP439, GLY8, TYR337, TYR341, TRP439, and ASP74 were forming hydrogen bonds, and TRP86, TRP439, TYR337, PRO446, and TYR449 were involved in hydrophobic interactions (Table 4). FCA's binding to the AChE (4BDT) active site was primarily regulated by interactions with TRP86, which formed one carbon-type hydrogen bond and two hydrophobic interactions (pi-pi stacking) between TRP86's indole sidechain and FCA. FCA has also been involved in van der Waals interactions with HIS447 and other nearby residues (Fig. 1).

Antibiotic Resistance

Antibiotics' effectiveness, which has revolutionized medicine and saved millions of lives, is under risk due to the global development of resistant bacteria. Bacterial illnesses have resurfaced decades after the initial patients received antibiotic treatment [22]. The most popular class of antibiotics is called β-lactams, and bacterial produced β-lactamase enzymes, which hydrolyze the β-lactam ring and render the medicine inactive, are the main source of β-lactam resistance. Two different types of β-lactamases, metallo-beta-lactamase NMD-1 from *Klebsiella pneumoniae* (PDB ID: 5ZGE) and beta-lactamase from *Citrobacter freundii* (PDB ID: 1FR6), were considered. The active site of beta-lactamase (1FR6) had a binding with HMF and its derivatives within a range of − 4.6 to − 6.4 kcal/mol. Mainly, residues SER64, GLU272, ALA298, LYS315, THR316, SER318, GLY317, and ASN346 were involved in hydrogen bonds and TYR150, MET265, and ALA292 were involved in hydrophobic interactions (Table 5). FCA interacted with conserved structural motifs in the active site (1FR6), forming 6 conventional hydrogen bonds with SER64, GLU272, LYS315, SER318, and ASN346, as well as one carbon-hydrogen bond with GLY317 and two hydrophobic interactions with TYR150 (pi-alkyl) and ALA298 (pi-pi stacking). In addition to these bonds, van der Waals interactions were formed with ARG148, LEU293, THR316, and GLY317 residues (Fig. 2). On the other hand, 5ZGE (New Delhi metallo-beta-lactamase) showed binding energy of − 3.7 to − 5.1 kcal/mol (Table 3). Residues HIS189, CYS208, LYS211, GLY219, ASN220, and HIS250 were involved in hydrogen bonds, and residues ASP124, CYS208, and HIS250 are involved in hydrophobic interactions (Table 5).

Antifungal

According to estimates, up to 150 million people could encounter an invasive fungal infection each year, and these infections are thought to be responsible for 1.5 million fatalities. This illness burden linked with fungal infections in humans is typically overlooked. There are currently only three major pharmacological classes of systemic antifungals that are approved for clinical use: triazoles, polyenes (represented by amphotericin B), and echinocandins. Resistance to antifungals is a significant issue given the few numbers of treatments and targets [23]. Azole antifungal medications target the

Table 2 ADMET profile of all the compounds made using pkCSM method

Property	Model name	HMF Predicted value	BHMF	DMF	EMF	EL	FDC	FCA	Unit
Absorption	Water solubility	−0.59	−1.261	−0.975	−0.937	−0.209	−0.039	−2.744	Numeric (log mol/L)
Absorption	Caco2 permeability	1.172	1.103	1.521	1.701	1.203	1.235	0.69	Numeric (log Papp in 10^{-6} cm/s)
Absorption	Intestinal absorption (human)	95.848	93.815	96.883	97.476	100	98.155	78.151	Numeric (% absorbed)
Absorption	Skin permeability	−3.416	−3.138	−2.226	−2.827	−2.703	−3.144	−2.735	Numeric (log Kp)
Absorption	P-glycoprotein substrate	No	No	Yes	No	No	No	No	Categorical (yes/no)
Absorption	P-glycoprotein I inhibitor	No	No	No	No	No	No	No	Categorical (yes/no)
Absorption	P-glycoprotein II inhibitor	No	No	No	No	No	No	No	Categorical (yes/no)
Distribution	VDss (human)	−0.146	−0.028	0.038	−0.172	−0.258	−0.293	−0.997	Numeric (log L/kg)
Distribution	Fraction unbound (human)	0.744	0.801	0.618	0.613	0.692	0.674	0.726	Numeric (Fu)
Distribution	BBB permeability	−0.361	−0.406	0.083	0.043	−0.202	−0.32	−0.226	Numeric (log BB)
Distribution	CNS permeability	−2.914	−2.967	−2.654	−3.137	−2.692	−2.933	−3.045	Numeric (log PS)
Metabolism	CYP2D6 substrate	No	No	No	No	No	No	No	Categorical (yes/no)
Metabolism	CYP3A4 substrate	No	No	No	No	No	No	No	Categorical (yes/no)

Table 2 (continued)

Property	Model name	HMF Predicted value	BHMF	DMF	EMF	EL	FDC	FCA	Unit
Metabolism	CYP1A2 inhibitor	No	No	No	No	No	No	No	Categorical (yes/no)
Metabolism	CYP2C19 inhibitor	No	No	No	No	No	No	No	Categorical (yes/no)
Metabolism	CYP2C9 inhibitor	No	No	No	No	No	No	No	Categorical (yes/no)
Metabolism	CYP2D6 inhibitor	No	No	No	No	No	No	No	Categorical (yes/no)
Metabolism	CYP3A4 inhibitor	No	No	No	No	No	No	No	Categorical (yes/no)
Excretion	Total clearance	0.614	0.656	0.65	0.716	0.852	0.561	0.663	Numeric (log ml/min/kg)
Excretion	Renal OCT2 substrate	No	No	No	No	No	No	No	Categorical (yes/no)
Toxicity	AMES toxicity (mutagenic or carcinogenic)	No	No	No	No	No	No	No	Categorical (yes/no)
Toxicity	Max. tolerated dose (human)	0.77	0.162	1.022	0.882	1.06	1.031	0.58	Numeric (log mg/kg/day)
Toxicity	hERG I inhibitor	No	No	No	No	No	No	No	Categorical (yes/no)
Toxicity	hERG II inhibitor	No	No	No	No	No	No	No	Categorical (yes/no)
Toxicity	Oral rat acute toxicity (LD50)	2.283	2.204	2.502	2.557	1.938	2.388	2.211	Numeric (mol/kg)

Table 2 (continued)

Property	Model name	HMF Predicted value	BHMF	DMF	EMF	EL	FDC	FCA	Unit
Toxicity	Oral rat chronic toxicity (LOAEL)	2.488	1.528	1.974	2.3	2.442	2.485	2.02	Numeric (log mg/kg_bw/day)
Toxicity	Hepatotoxicity	No	No	No	Yes	No	No	No	Categorical (yes/no)
Toxicity	Skin sensitization	No	No	Yes	Yes	Yes	No	No	Categorical (yes/no)
Toxicity	*T. pyriformis* toxicity	−0.767	−0.705	−0.353	−0.352	−0.503	−0.852	0.179	Numeric (log µg/L)
Toxicity	Minnow toxicity	2.836	3.133	2.033	1.88	2.151	2.539	3.062	Numeric (log mM)

Table 3 Binding affinities of compounds of interest (ligands) with specific targets (proteins)

	PDB ID	Receptor	HMF	BHMF	DMF	EL	EMF	FCA	FDC
A	Alzheimer targets								
1	4BDS	Human butyrylcholinesterase	−5.3	−5.1	−4.7	−5.1	−5.6	−6.1	−5.2
2	6NCN	Apolipoprotein E4	−4.1	−4.2	−3.8	−4.1	−4.6	−4.8	−4.2
3	4IVT	β-Secretase (BACE1)	−4.7	−4.4	−4.2	−4.4	−4.9	−5.2	−4.4
4	4BDT	Human acetylcholinesterase	−5.3	−5.4	−5.3	−5.2	−5.6	−6.2	−5.3
B	Antibiotic resistance								
5	1FR6	Beta-lactamase	−5.6	−5.6	−4.6	−5.1	−5.6	−6.4	−5.3
6	5ZGE	New Delhi metallo-beta-lactamase	−4.5	−4.4	−3.7	−4.4	−4.5	− 5.1	− 4.2
C	Antifungal								
7	4WMZ	*S. cerevisiae* CYP51	−5.1	−5.2	−4.7	−4.9	−5.4	−5.9	−4.9
D	Anti-quorum sensing								
8	1H0M	Quorum sensing protein Trar	−5.2	−5.1	−5.3	−5.7	−5.9	−6	−5.3
9	1L3L	Bacterial quorum sensing transcription factor (*Agrobacterium*)	−5.3	−5.2	−5.6	−5.6	−5.7	−5.9	−5.3
10	4LFU	SdiA, a quorum sensing receptor *E. coli*	−5.1	−5	−4.9	−5.3	−5.7	−5.7	−5.1
11	2UV0	*P. aeruginosa* LasR	−5.7	−5.6	−5.1	−6.2	−6.3	−7	−5.8
12	3QP1	Crystal structure of CviR	−5.3	−5.2	−5.1	−5.6	−5.6	−5.7	−5.2
E	Antimicrobial								
13	1JIJ	*S. aureus* tyrosyl-tRNA synthetase	−5.7	−5.4	−4.5	−5.3	−5.8	−6.7	−5.6
14	1KZN	*E.coli* DNA gyrase	−4.9	−4.9	−4.3	−4.8	−5.1	−5.6	−5.6
15	2MLM	Sortase A from *S. aureus*	−4	−4	−3.8	−3.8	−4.1	−4.6	−3.8
16	2XCT	*S. aureus* gyrase	−3.9	−3.9	−3.3	−3.7	−4.1	−4.5	−3.9
17	3FRA	*S. aureus* dihydrofolate reductase	−5	−5	−4.3	−4.7	−5.3	−6	−4.9
18	4URM	*S. aureus* gyrase B 24 kDa	−5	−5.1	−4	−4.9	−5.2	− 5.9	−4.9
F	Antiviral								
19	2GV9	HSV type 1 DNA polymerase	−4.1	−4.1	−3.5	−3.9	−4.3	− 4.6	−3.7
20	2KI5	HSV TYPE-1 thymidine kinase	−5.2	−5.2	−4.8	−5.4	−5.7	−6	−5.3
21	5GMZ	Hepatitis B virus core protein (Capsid)	−4	−4.3	−3.6	−4.1	−4.2	−4.8	−4
22	4A92	Hepatitis C virus NS3-4A protease-helicase	−4.9	−4.8	−3.8	−4.7	−4.6	−5.6	−4.5
23	2GZ7	SARS-CoV main protease	−4.2	−4.6	−3.6	−4	−4.3	−5	−4
24	6P9A	HIV protease	−4.1	−4.1	−3.7	−4.5	−4.7	−4.9	−4.2
25	4P16	Papain-like protease of MERS coronavirus	−3.6	−3.9	−3	−2.9	−3.6	−4.1	−3.5
26	6LU7	COVID-19 main protease	−4.4	−4.5	−3.8	−4.1	−4.4	−5.2	−4.3
27	7NNG	SARS-CoV-2 helicase	−5.1	−4.9	−3.6	−4.5	−4.9	−6	−5

fungal cytochrome P450 lanosterol 14α-demethylase (CYP51), which is necessary for the manufacture of ergosterol that is unique to fungi. Despite CYP51's demonstrated effectiveness as a therapeutic target for azole antifungals, it is urgently needed to create new antifungals that specifically target CYP51 in order to combat pathogenic fungi's resistance to azole medications [24, 25]. *S. cerevisiae* CYP51 (PDB ID: 4WMZ)

Table 4 Alzheimer target protein's residues involved in docking and interaction with ligand (hydrogen bond, hydrophobic, and electrostatic interactions)

Ligand	PDB ID	ΔG_b (binding energy), kcal/mol	Hydrogen bonds		Hydrophobic and electrostatic interactions		
			Interacting residues	Distance	Type	Interacting residues	Distance
HMF	4BDS	−5.3	GLY116	2.49096	Pi-anion	GLU197	4.84757
			GLY117	2.27791	Pi-pi T-shaped	TRP82	5.73984
			TYR128	2.32438	Pi-pi T-shaped	HIS438	5.09827
			GLU197	3.40772	Pi-pi T-shaped	TRP82	5.32087
	4BDT	−5.3	THR83	2.88375	Pi-pi stacked	TRP86	3.94617
			TRP86	3.79164	Pi-pi stacked	TRP86	4.82974
					Pi-pi stacked	TYR337	3.78461
BHMF	4BDS	−5.1	GLY116	2.85548	Pi-pi T-shaped	HIS438	4.76455
			GLY117	2.78655			
			GLY117	2.51097			
			SER198	2.03622			
			ALA199	2.65682			
			GLU197	2.48582			
			SER198	3.52174			
			TRP231	2.96304			
	4BDT	−5.4	TRP439	2.74238	Pi-pi stacked	TRP86	3.8646
			GLY82	2.91331	Pi-pi stacked	TRP86	4.87653
					Pi-pi stacked	TYR337	3.98445
DMF	4BDT	−5.3			Pi-sigma	TRP86	3.95142
					Pi-sigma	TRP86	3.86149
					Pi-sigma	TRP439	3.88638
					Pi-pi stacked	TRP86	4.15405
					Pi-pi stacked	TRP86	4.99294
					Pi-pi stacked	TYR337	3.65927
					Alkyl	PRO446	4.81719
					Pi-alkyl	TYR337	4.76084
					Pi-alkyl	TYR337	4.22786
					Pi-alkyl	TRP439	4.24735
					Pi-alkyl	TYR449	4.97142
EL	4BDS	−5.1	GLY116	2.2721	Pi-sigma	TRP231	3.63003
			GLY117	2.33495	Pi-alkyl	HIS438	4.40406
			SER198	2.2629			
	4BDT	−5.2	THR83	2.64433	Pi-sigma	TYR337	3.86108
			TRP86	2.18542	Pi-sigma	TRP86	3.94739
			TYR337	2.91584			
			TYR341	2.50088			
			TRP439	2.73181			
EMF	4BDS	−5.6	GLY116	2.99936	Pi-sigma	TRP82	3.85459
			GLY117	2.63906	Pi-pi T-shaped	HIS438	5.00484
			SER198	2.05982	Pi-alkyl	TRP82	4.80042
			ALA199	2.7129			
			SER198	3.59105			
	4BDT	−5.6	THR83	2.13538	Pi-pi stacked	TRP86	3.98462
			TRP86	3.67529	Pi-pi stacked	TRP86	4.8994
					Pi-pi stacked	TYR337	3.77269

Table 4 (continued)

Ligand	PDB ID	ΔG_b (binding energy), kcal/mol	Hydrogen bonds		Hydrophobic and electrostatic interactions		
			Interacting residues	Distance	Type	Interacting residues	Distance
FCA	4BDS	−6.1	GLY116	2.46458	Pi-anion	GLU197	4.40575
			GLY117	2.2676	Pi-pi T-shaped	TRP82	5.70176
					Pi-pi T-shaped	TRP82	5.2995
	4IVT	−5.2	GLN73	2.35805			
			GLN73	2.74925			
			GLN73	3.03544			
			ASP228	3.02051			
			THR231	3.46032			
	4BDT	−6.2	THR83	2.74393	Pi-pi stacked	TRP86	4.15722
			ASP74	3.0264	Pi-pi stacked	TRP86	5.14368
			TYR341	2.03397	Pi-pi stacked	TYR337	3.66011
FDC	4BDS	−5.2	GLY116	2.4778	Pi-anion	GLU197	4.89603
			GLY117	2.2093	Pi-pi T-shaped	TRP82	5.86536
			GLU197	3.44895	Pi-pi T-shaped	HIS438	5.03604
					Pi-pi T-shaped	TRP82	5.48006
	4BDT	−5.3	THR83	2.18608	Pi-pi stacked	TRP86	4.07918
			TRP86	3.69757	Pi-pi stacked	TRP86	4.99457
			HIS447	3.52688	Pi-pi stacked	TYR337	3.7365

is used as a target to study the antifungal potential of HMF and its derivatives. CPY51 (4WMZ) showed binding energy of −4.7 to −5.9 kcal/mol (Table 3) with residues GLY310, GL7Y314, HIS381, SER382, PHE506, THR507, and SER508 participating in hydrogen bonds and MET509, LEU380, VAL510, PHE236, and PRO238 were involved in hydrophobic interactions (Table 6).

Anti-quorum Sensing

Quorum sensing (QS) is an intercellular communication method used by bacteria. It is dependent on the density of bacterial cells and regulates the expression of genes, including those that determine virulence, to govern the pathogenesis of several organisms. Innovative anti-infective drugs that do not rely on the usage of antibiotics are being developed, and QS has emerged as a promising target. In our study, we used the following target for evaluating the anti-quorum sensing activity of HMF and its derivatives: quorum sensing protein TraR (PDB ID: 1H0M), bacterial quorum sensing transcription factor (PDB ID: 1L3L), *Escherichia coli* SdiA (PDB ID: 4LFU), *P. aeruginosa* LasR ligand-binding domain (PDB ID: 2UV0), CviR ligand-binding domain (PDB ID: 3QP1). TraR had binding energy of −5.1 to −6 kcal/mol with residues TRP57, TYR61, ASP70, TYR53, and THR129 interacted with hydrogen bond formation, and residues TYR61, TYR53, ALA38, LEU40, TRP57, VAL72, ILE110, and TRP85 were involved in hydrophobic interactions (Table 7). 1L3L had similar binding energies ranging in between −5.2 and −5.9 kcal/mol and residues TYR61, TRP57, ASP70, GLN58, TYR53, and THR129 were involved in hydrogen bond formation, where else TYR61, LEU40, ALA49, TYR53, TRP57, TYR61, VAL72, ILE110, and ASP70 were involved in hydrophobic interactions (Table 7). SdiA (4LFU) had

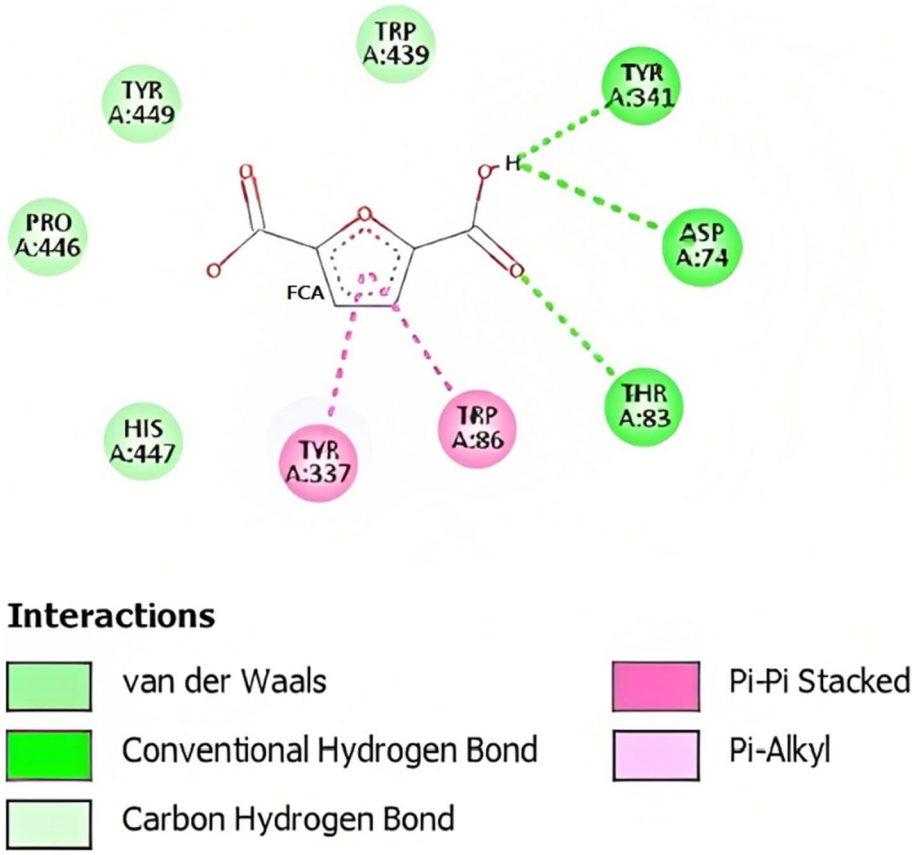

Fig. 1 Two-dimensional plot of the interaction of compound FCA with the active site of acetylcholinesterase (4BDT)

a range of −4.9 to −5.7 kcal/mol binding energy (Table 3) with our compounds. Residues like TYR63, ALA109, ALA110, TRP107, and ARG117 were involved in hydrogen bond formation and residues TRP67, TYR63, ALA110, HIS113, VAL68, TYR71, PHE100, LEU115, ARG116, and ARG111 were involved in hydrophobic interactions (Table 7). LasR (2UV0) had shown stronger binding energy with our compounds ranging from −5.1 to −7 kcal/mol (Table 3). Residues SER129, LEU110, THR75, and TYR56 were involved in hydrogen bond formation and ASP73, TYR56, ALA105, LEU110, TPR88, PHE101, LEU36, and TYR64 were involved in hydrophobic interactions (Table 7). When FCA docked with LasR (2UV0), the active site residues TYR56, TYR64, TYR93, LEU110, and SER129 established six hydrogen bonds. It also interacted hydrophobically with ALA105 and LEU110; electrostatically with ASP73; and van der Waals interactions with LEU36, TRP60, THR75, VAL76, TRP88, ILE92, and PHE101 (Fig. 3). Apart from FCA, EMF and HMF were also found to be interacting with active site residues. HMF formed a hydrogen bond with SER129, an electrostatic bond with ASP73, and hydrophobic interactions with TYR56 (Table 7), where else EMF also had a hydrogen bond with SER129 and an electrostatic interaction with ASP73 (Table 7). 3QP1 had a narrow range of binding energy with our compounds, −5.1 to −5.7 kcal/mol (Table 3). Residues TYR80 and MET135 were

Table 5 Antibiotic resistance protein's residues involved in docking and interaction with ligand (hydrogen bond, hydrophobic, and electrostatic interactions)

Ligand	PDB ID	ΔG_b (binding energy), kcal/mol	Hydrogen bonds		Hydrophobic and electrostatic interactions		
			Interacting Residues	Distance	Type	Interacting Residues	Distance
HMF	1FR6	−5.6	LYS315	2.93672	Pi-pi stacked	TYR150	3.96411
			THR316	2.70721	Pi-alkyl	ALA292	5.02053
			ASN346	3.20839			
			THR316	2.40085			
BHMF	1FR6	−5.6	LYS315	2.62669	Pi-pi stacked	TYR150	3.88839
			LYS315	2.33903	Pi-alkyl	ALA292	5.01624
			ASN346	2.16215			
EL	1FR6	−5.1	LYS315	2.23803	Pi-sigma	TYR150	3.72773
			SER318	2.37765			
			ASN346	2.23151			
EMF	1FR6	−5.6	LYS315	2.68059	Pi-pi stacked	TYR150	3.99259
			LYS315	2.37555	Alkyl	ALA292	4.14945
			ASN346	2.22355	Alkyl	MET265	5.21423
			GLU272	3.38169	Pi-alkyl	ALA292	5.0672
			ALA298	3.57384			
FCA	1FR6	−6.4	SER64	2.74711	Pi-pi stacked	TYR150	4.00119
			LYS315	2.77237	Pi-alkyl	ALA292	5.07531
			LYS315	2.49357			
			LYS315	2.05748			
			SER318	2.81151			
			ASN346	2.00429			
			GLU272	2.43713			
			GLY317	3.34363			
	5ZGE	−5.1	CYS208	3.77165	Pi-cation	HIS250	3.78908
			LYS211	1.84271	Pi-anion	ASP124	3.74251
			ASN220	2.02969	Pi-pi stacked	HIS250	4.63876
			HIS189	3.49838	Pi-alkyl	CYS208	5.06554
			GLY219	3.70515			
			HIS250	3.6069			
FDC	1FR6	−5.3	LYS315	2.78931	Pi-pi stacked	TYR150	4.08654
			LYS315	2.56818	Pi-alkyl	ALA292	5.17947
			LYS315	2.14767			
			ANS346	2.17846			

only involved in hydrogen bond formation and ASP97, TYR80, TRP111, ILE99, ALA130, MET135, PHE115, and PHE126 were involved in hydrophobic interactions (Table 7).

Antimicrobial

The discovery of new and potent antimicrobial chemicals is necessary due to the continual evolution of bacterial resistance to currently used antibiotics. Additionally, there is a need for effective and affordable antimicrobial substances. In the current study, some crucial enzymes (*S. aureus* tyrosyl-tRNA synthetase (PDB ID: 1JIJ), *E. coli* DNA gyrase (PDB ID: 1KZN), *S. aureus* dihydrofolate reductase (PDB ID: 3FRA), *S. aureus* gyrase B 24 kDa (PDB ID: 4URM), *S. aureus* gyrase (PDB ID: 2XCT), and

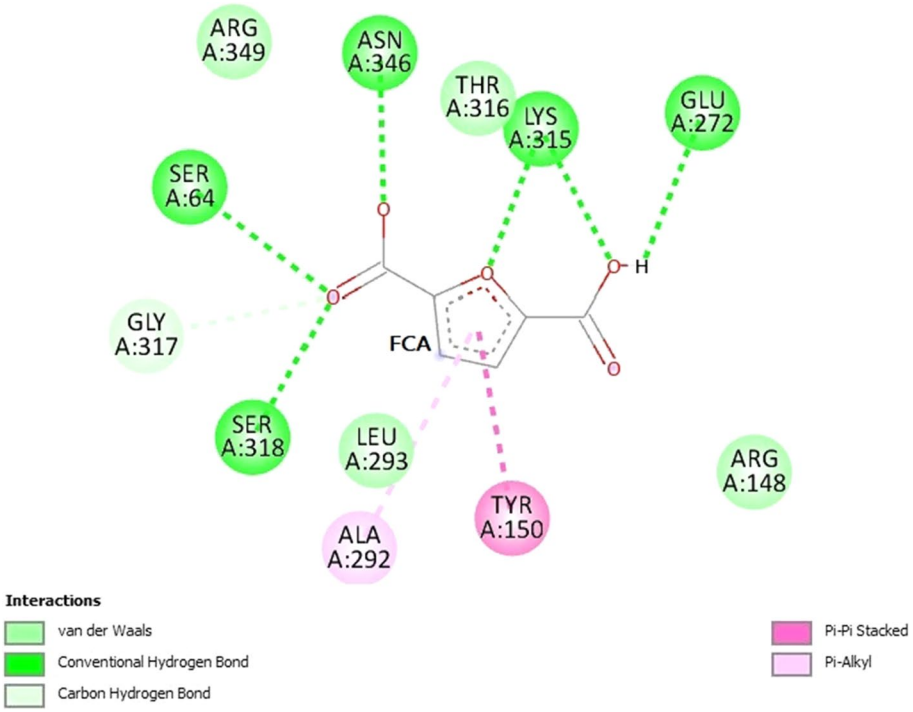

Fig. 2 Two-dimensional plot of the interaction of compound FCA with the active site of β-Lactamase (1FR6)

sortase A from *S. aureus* (PDB ID: 2MLM)) for microbial growth were targeted to examine the antimicrobial potential of our compound of interests. The minimum binding energy of − 5.7 kcal/mol, − 5.4 kcal/mol, − 4.5 kcal/mol, − 5.3 kcal/mol, − 5.8 kcal/

Table 6 Antifungal target protein's residues involved in docking and interaction with ligand (hydrogen bond, hydrophobic, and electrostatic interactions)

Ligand	PDB ID	ΔG_b (binding energy), kcal/mol	Hydrogen bonds		Hydrophobic and electrostatic interactions		
			Interacting residues	Distance	Type	Interacting residues	Distance
HMF	4WMZ	− 5.1	HIS381 SER382 PHE506 THR507	3.04614 2.88989 2.42193 3.63893	Pi-alkyl Pi-alkyl	PRO238 MET509	5.03395 5.09487
BHMF	4WMZ	− 5.2	HIS381 THR507	2.67489 3.67482	Pi-alkyl Pi-alkyl	PRO238 MET509	5.14651 5.02774
EMF	4WMZ	− 5.4	GL7Y314 GLY310	3.77911 3.39318	Alkyl Alkyl Pi-alkyl	LEU380 VAL510 PHE236	5.10129 5.02803 5
FCA	4WMZ	− 5.9	HIS381 SER508 SER382	2.34791 2.75076 2.74016	Pi-alkyl	MET509	5.21456

Table 7 Anti-quorum sensing protein's residues involved in docking and interaction with ligand (hydrogen bond, hydrophobic, and electrostatic interactions)

Ligand	PDB ID	ΔG_b (binding energy), kcal/mol	Hydrogen bonds		Hydrophobic and electrostatic interactions		
			Interacting residues	Distance	Type	Interacting residues	Distance
HMF	1H0M	−5.2	TYR61	3.01571	Pi-pi stacked	TYR61	3.79437
			ASP70	2.3576	Pi-pi T-shaped	TYR53	4.90411
					Pi-alkyl	ALA38	4.7175
					Pi-alkyl	LEU40	5.0641
	1L3L	−5.3	TYR61	2.75667	Pi-pi stacked	TYR61	3.60455
			TRP57	3.23489	Pi-alkyl	LEU40	4.85395
					Pi-alkyl	ALA49	5.49176
	4LFU	−5.1	ALA109	2.19142	Pi-sigma	TRP67	3.9532
					Pi-pi T-shaped	TYR63	5.21037
					Pi-alkyl	ALA110	4.95338
	2UV0	−5.7	SER129	1.93377	Pi-anion	ASP73	3.83796
					Pi-pi T-shaped	TYR56	5.13403
					Pi-alkyl	ALA105	5.28543
					Pi-alkyl	LEU110	4.97725
	3QP1	−5.3	TYR80	2.34968	Pi-anion	ASP97	3.36918
					Pi-donor hydrogen bond	TYR80	3.1661
					Pi-pi stacked	TRP111	5.79598
					Pi-pi stacked	TRP111	4.71127
					Pi-alkyl	ILE99	5.00873
BHMF	1HOM	−5.1	ASP70	2.4046	Pi-pi stacked	TYR61	3.91131
					Pi-pi T-shaped	TYR53	4.7281
					Pi-alkyl	ALA38	4.45372
					Pi-alkyl	LEU40	4.96248
	1L3L	−5.2	ASP70	2.49153	Pi-pi stacked	TYR61	3.603
			GLN58	3.2782	Pi-alkyl	LEU40	4.92841
	4LFU	−5	TYR6	3.2167	Pi-sigma	TRP67	3.9247
					Pi-pi T-shaped	TYR63	5.28805
					Pi-alkyl	ALA110	5.02131
	2UV0	−5.6	LEU11	3.5078	Pi-anion	ASP73	3.79527
					Pi-Pi T-shaped	TYR56	5.11981
					Pi-alkyl	ALA105	5.29375
					Pi-alkyl	LEU110	5.00338
	3QP1	−5.2	TYR80	2.3068	Pi-anion	ASP97	3.33619
			MET135	2.10258	Pi-pi stacked	TRP111	5.77829
			TYR80	3.15672	Pi-pi stacked	TRP111	4.71534
					Pi-alkyl	ILE99	4.95324

Table 7 (continued)

Ligand	PDB ID	ΔG_b (binding energy), kcal/mol	Hydrogen bonds		Hydrophobic and electrostatic interactions		
			Interacting residues	Distance	Type	Interacting residues	Distance
DMF	1HOM	−5.3	TRP57	3.08593	Pi-pi stacked	TYR61	3.75502
					Pi-pi T-shaped	TYR53	4.79545
					Pi-alkyl	TYR53	4.99979
					Pi-alkyl	TYR53	5.07606
					Pi-alkyl	TRP57	4.24194
					Pi-alkyl	TYR61	4.25474
					Pi-alkyl	TYR61	4.38833
					Pi-alkyl	ALA38	4.65269
					Pi-alkyl	LEU40	5.11256
	1L3L	−5.6			Pi-pi stacked	TYR61	3.70217
					Alkyl	LEU40	4.43069
					Pi-alkyl	TYR53	5.07222
					Pi-alkyl	TRP57	4.06598
					Pi-alkyl	TYR61	4.64648
					Pi-alkyl	TYR61	4.16966
					Pi-alkyl	LEU40	4.99699
					Pi-alkyl	ALA49	5.1077
	2UV0	−5.1			Pi-anion	ASP73	3.86226
					Pi-sigma	TRP88	3.61571
					Pi-Pi T-shaped	TYR56	5.2341
					Alkyl	ALA105	4.00889
					Alkyl	LEU110	4.84257
					Pi-alkyl	TYR56	5.23784
					Pi-alkyl	TPR88	4.28259
					Pi-alkyl	PHE101	5.43148
					Pi-alkyl	ALA105	5.1333
					Pi-alkyl	LEU110	4.93828
	3QP1	−5.1			Pi-anion	ASP97	3.50076
					Pi-pi stacked	TRP111	5.72198
					Pi-pi stacked	TP111	4.57044
					Alkyl	ALA130	3.95881
					Alkyl	ILE99	4.29892
					Alkyl	MET135	5.47326
					Pi-alkyl	TRP111	5.12894
					Pi-alkyl	TRP111	4.87396
					Pi-alkyl	TRP111	4.1125
					Pi-alkyl	PHE115	4.8209
					Pi-alkyl	PHE126	4.9202
					Pi-alkyl	ILE99	5.13182

Table 7 (continued)

Ligand	PDB ID	ΔG_b (binding energy), kcal/mol	Hydrogen bonds		Hydrophobic and electrostatic interactions		
			Interacting residues	Distance	Type	Interacting residues	Distance
EL	1H0M	−5.7	TYR53	2.42449			
			TRP57	2.39259			
			THR129	1.89874			
	1L3L	−5.6			Alkyl	VAL72	4.49964
					Pi-alkyl	TYR53	5.41779
	4LFU	−5.3	ALA110	3.51413	Pi-sigma	HIS113	3.66428
					Alkyl	VAL68	4.44701
					Pi-alkyl	TYR63	4.27691
					Pi-alkyl	TYR71	5.10787
	2UV0	−6.2			Pi-sigma	TRP88	3.72571
					Alkyl	LEU36	3.94813
					Pi-alkyl	TYR56	5.16141
					Pi-alkyl	TYR64	4.15691
	3QP1	−5.6	TYR80	2.34288	Pi-sigma	TYR88	3.74391
			TRP84	2.33691	Alkyl	LEU57	4.71439
			SER155	2.24942	Alkyl	LEU85	5.10701
					Pi-alkyl	TYR80	5.05972

Table 7 (continued)

Ligand	PDB ID	ΔG_b (binding energy), kcal/mol	Hydrogen bonds		Hydrophobic and electrostatic interactions		
			Interacting residues	Distance	Type	Interacting residues	Distance
EMF	1H0M	−5.9	TRP57	2.67857	Pi-pi stacked	TYR61	3.6369
			TRP57	1.91812	Pi-pi T-shaped	TYR53	4.64087
			ASP70	3.26528	Alkyl	VAL72	4.91859
					Alkyl	ILE110	5.12124
					Pi-alkyl	TRP85	4.42395
					Pi-alkyl	ALA38	4.70623
					Pi-alkyl	LEU40	5.407
	1L3L	−5.7	TYR53	2.21872	Pi-anion	ASP70	3.51557
					Pi-alkyl	VAL72	5.052
					Pi-alkyl	ILE110	5.21814
	4LFU	−5.7			Pi-pi stacked	PHE100	4.40549
					Pi-alkyl	ALA110	3.70155
					Pi-alkyl	LEU115	5.35353
	2UVO	−6.3	THR75	2.12572	Pi-anion	ASP73	3.37713
			SER129	2.28893	Pi-sigma	TRP88	3.60595
			SER129	2.84066	Pi-pi stacked	TYR64	5.23312
					Pi-alkyl	LEU36	4.86369
	3QP1	−5.6	TRP84	2.28441	Pi-anion	ASP97	3.48774
			TYR80	2.74015	Pi-pi T-shaped	TRY80	5.23612
					Alkyl	ALA59	3.785
					Alkyl	LEU57	4.99279
					Alkyl	LEU72	4.85294
					Alkyl	LEU100	4.74633
					Pi-alkyl	ILE99	5.04316

Table 7 (continued)

Ligand	PDB ID	ΔG_b (binding energy), kcal/mol	Hydrogen bonds		Hydrophobic and electrostatic interactions		
			Interacting residues	Distance	Type	Interacting residues	Distance
FCA	1H0M	−6	TRP57	3.02265	Pi-pi stacked	TYR61	3.6445
			TRP57	2.14358	Pi-pi T-shaped	TYR53	4.79732
			ASP70	2.66633	Pi-alkyl	ALA38	4.66416
			TRP57	3.41207	Pi-alkyl	LEU40	5.13111
	1L3L	−5.9	THR129	2.09716	Pi-anion	ASP70	3.33512
					Pi-alkyl	VAL72	4.91952
	4LFU	−5.7	TRP107	2.95547	Amide-pi stacked	ARG116	3.76205
			ARG117	2.85772	Pi-alkyl	ARG111	5.15816
	2UV0	−7	TYR56	2.48042	Pi-anion	ASP73	3.57952
			SER129	2.19407	Pi-alkyl	ALA105	5.47159
			LEU110	2.85645	Pi-alkyl	LEU110	5.25242
	3QP1	−5.7	TYR80	2.75254	Pi-donor	ASP97	3.44253
					Pi-pi T-shaped	TYR80	5.29129
					Pi-alkyl	ILE99	4.94795
FDC	1H0M	−5.3	TRP57	2.07268	Pi-pi stacked	TYR61	3.63098
					Pi-pi T-shaped	TYR53	4.84628
					Pi-alkyl	ALA38	4.71274
					Pi-alkyl	LEU40	5.11691
	1L3L	−5.3	TYR53	2.14832	Pi-anion	ASP70	3.43543
			THR129	2.85498	Pi-alkyl	VAL72	5.00644
					Pi-alkyl	ILE110	5.31483
	4LFU	−5.1			Pi-Pi T-shaped	TYR63	5.01938
					Pi-pi T-shaped	TRP67	5.21139
					Pi-alkyl	ALA110	5.046
	2UV0	−5.8	SER129	1.83558	Pi-anion	ASP73	3.84525
					Pi-pi T-shaped	TYR56	5.21849
					Pi-alkyl	ALA105	5.20745
					Pi-alkyl	LEU110	4.97167
	3QP1	−5.2	TYR80	3.13457	Pi-anion	ASP97	3.35817
					Pi-pi stacked	TRP111	5.88849
					Pi-pi stacked	TRP111	4.80049
					Pi-alkyl	ILE99	5.06541

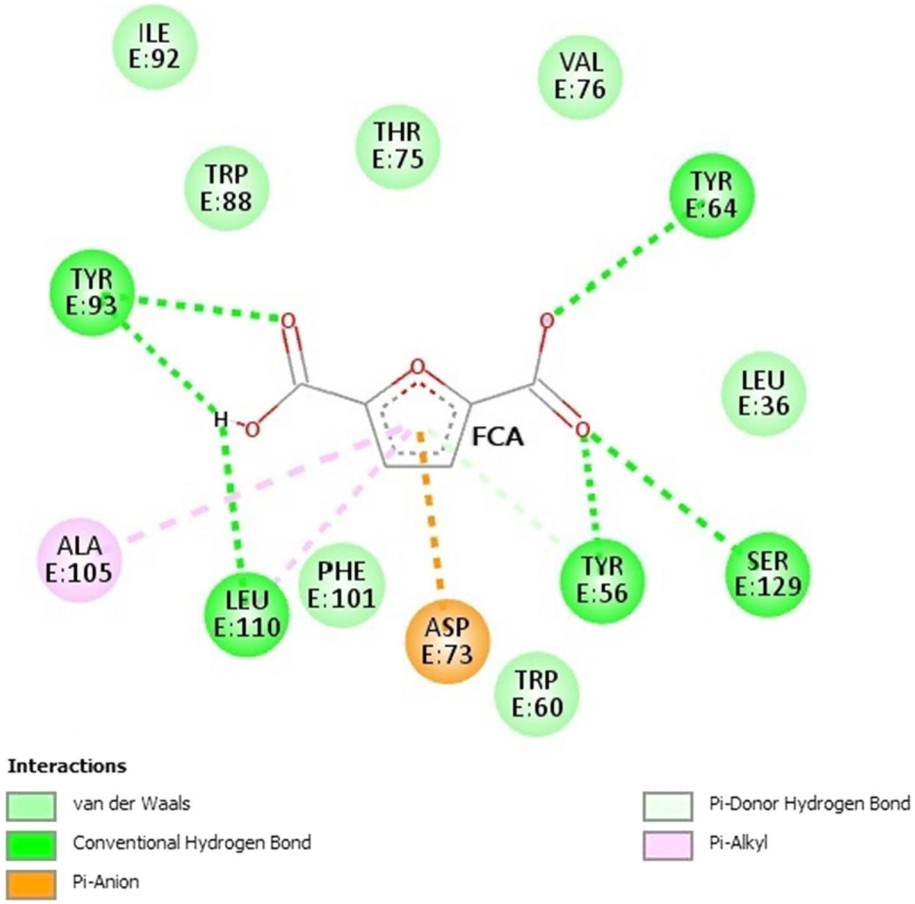

Fig. 3 Two-dimensional plot of the interaction of compound FCA with the active site of LasR (2UVO)

mol, − 6.7 kcal/mol, and − 5.6 kcal/mol was recorded for HMF, BHMF, DMF, EL, FCA, and FDA respectively (Table 3). With tyrosyl-tRNA synthetase (1JIJ), the binding energy ranged from − 4.5 to − 6.7 kcal/mol (Table 3) and residues GLY38, CYS37, THR75, GLN174, and ASP177 were involved in hydrogen bond formation and only LEU70 was found to be forming hydrophobic interactions (Table 8). FCA had the best binding energy (− 6.7 kcal/mol). It made six hydrogen connections with CYS37, GLY38, THR75, TYR170, GLN174, and GLN190 residues, as well as one hydrophobic interaction with LEU70 (Fig. 4). Aside from these, van der Waals interactions were seen with residues TYR36, ALA39, ASP40, ASN124, ASP177, GLN196, and ILE200 (Fig. 4). HMF had an important hydrogen bond with GLN174, hydrophobic interaction with ASP177, and van der Waals interactions with the other important residues in this domain. 1KZN's binding energy ranged from − 4.3 to − 5.6 kcal/mol (Table 3) and residues like GLY77 and THR165 were mainly involved in hydrogen bonds and residues ILE78, ASN46, ALA47, THR165, and ALA47 interacted with hydrophobically (Table 8). 3FRA had a − 4.3 to − 6 kcal/mol of binding energy (Table 3) with residues THR46, GLN95, THR96, ASN18, SER49, and GLY94 in hydrogen bond formation and

Table 8 Antimicrobial target protein's residues involved in docking and interaction with ligand (hydrogen bond, hydrophobic, and electrostatic interactions)

S. no	PDB ID	ΔG_b (binding energy), kcal/mol	Hydrogen bonds		Hydrophobic and electrostatic interactions		
			Interacting residues	Distance	Type	Interacting residues	Distance
HMF	1JIJ	−5.7	GLY38 GLN174 ASP177	2.12161 2.72211 3.35411	Pi-alkyl	LEU70	4.9106
	3FRA	−5	THR46 THR46 GLN95 THR96 ASN18 SER49	3.07838 2.02873 2.95644 2.14507 2.12733 3.6278	Pi-alkyl	LYS45	4.06219
	4URM	−5	GLY85 ILE51	2.30154 2.66942	Pi-alkyl	ILE86	4.48848
BHMF	1JIJ	−5.4	GLY38 ASP177	2.12442 3.33862	Pi-alkyl	LEU70	4.90923
	3FRA	−5	THR46 THR46 GLY94 ASN18 SER49	1.97951 2.01617 2.33053 2.74043 3.56611	Pi-alkyl	LYS45	4.10781
	4URM	−5.1	THR173 GLU58 SER55 ASP81	2.45726 2.75709 2.29257 2.14143	Pi-alkyl	ILE86	4.5304
EL	1JIJ	−5.3	GLN174	2.96333			
EMF	1JIJ	−5.8	GLY38 GLN174 VAL191 ASP177	2.3241 2.68262 3.52455 3.26564	Alkyl Pi-alkyl	CYS37 LEU70	4.62611 4.84469
	1KZN	−5.1	GLY77	2.2903	Pi-alkyl	ILE78	4.59044
	3FRA	−5.3	THR46 THR46 GLN95 THR96	3.05055 2.04492 2.93035 2.14777	Pi-alkyl	LYS45	4.08646
	4URM	−5.2	GLY85 THR173	2.31683 2.50639	Alkyl Alkyl Pi-alkyl	VAL79 ILE175 ILE86	4.53983 4.54516 4.57001
FCA	1JIJ	−6.7	THR75	2.12408	Pi-alkyl	LEU70	4.96089
	1KZN	−5.6			Amide-pi stacked Pi-alkyl	ASN46, ALA47 ILE78	4.41149 4.92107
	3FRA	−6.0	THR46 THR46 THR46 THR96 SER49	2.38996 1.99496 2.18855 2.43264 3.57557	Pi-alkyl	LYS45	3.98496
	4URM	−5.9	GLY85	2.20751	Pi-alkyl	ILE86	4.54959

Table 8 (continued)

S. no	PDB ID	ΔG_b (binding energy), kcal/mol	Hydrogen bonds		Hydrophobic and electrostatic interactions		
			Interacting residues	Distance	Type	Interacting residues	Distance
FDC	1JIJ	−5.6	CYS37 GLY38 GLN174 ASP177	3.66995 2.29384 2.7948 3.48245	Pi-alkyl	LEU70	4.84819
	1KZN	−5.6	THR165	2.31761	Pi-sigma Pi-alkyl	THR165 ALA47	3.68832 4.97394

only LYS45 was found in a hydrophobic interaction (Table 8). 4URM had a range of −4 to −5.9 kcal/mol (Table 3) of binding energy with residues GLY85, ILE51, THR173, GLU58, SER55, and ASP81 involved in hydrogen bond formation, and ILE86, VAL79, and ILE175 involved in hydrophobic interactions. 2MLM had binding energy of −3.8 to −4.6 kcal/mol (Table 3) and residues LEU111, LYS117, and ASN56 formed hydrogen bonds, and THR122 formed hydrophobic bonds (Table 8). 2XCT had binding

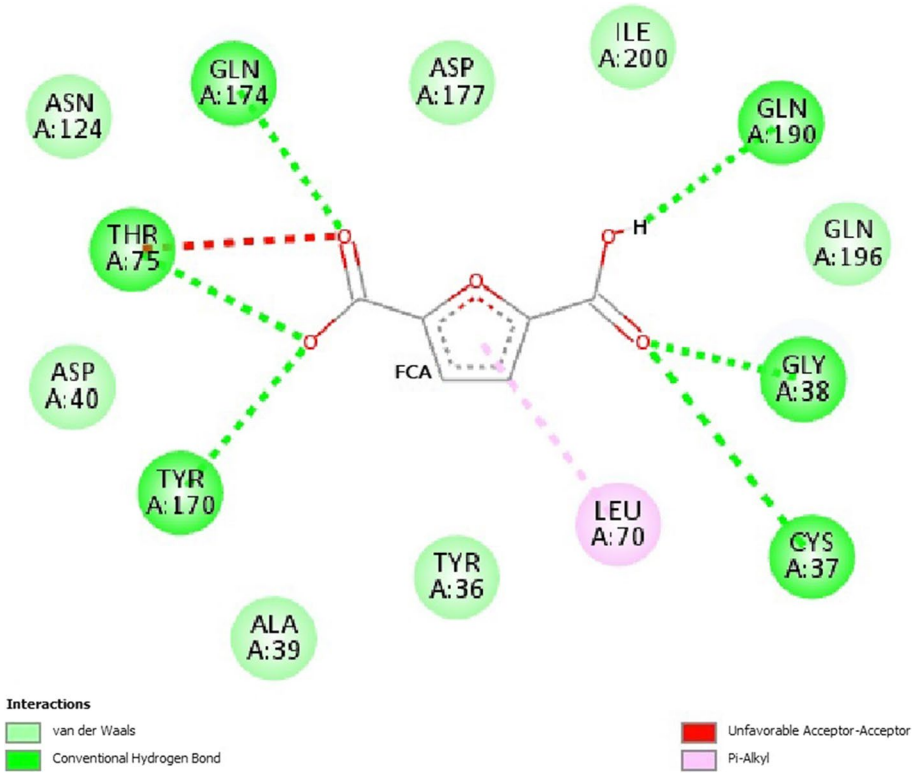

Fig. 4 Two-dimensional plot of the interaction of compound FCA with the active site of Tyrosyl-tRNA synthetase (1JIJ)

energy of − 4.3 to − 5.6 kcal/mol (Table 3) forming hydrophobic interactions mainly with residues VAL43, ALA47, GLU50, ASP73, GLY75, ARG76, GLY77, PRO79, THR165, and ASN46, and ILE78 involved in hydrophobic interactions (Table 8).

Antiviral

Numerous severe human diseases are brought on by viral infections, which are a burden for global health. Since viruses are capable of constant evolution, which results in drug-resistant mutations that render antiviral medications useless, treating viral illnesses is typically a challenging task. In pursuit of finding a potential antiviral candidate, we used several viral enzymes from some crucial viruses: HSV type 1 DNA polymerase (PDB ID: 2GV9), HSV TYPE-1 thymidine kinase (PDB ID: 2KI5), hepatitis B virus core protein (PDB ID: 5GMZ), hepatitis C virus NS3-4A protease-helicase (PDB ID: 4A92), SARS-CoV main protease (PDB ID: 2GZ7), HIV protease (PDB ID: 6P9A), papain-like protease of MERS coronavirus (PDB ID: 4P16), COVID-19 main protease (PDB ID: 6LU7), SARS-CoV-2 helicase (PDB ID: 7NNG). Out of all targets, HSV TYPE-1 thymidine kinase (2KI5) and SARS-CoV-2 helicase (7NNG) seem receptive to our compounds of interest. Thymidine kinase had binding energy of − 4.8 to − 6 kcal/mol (Table 3) with residues GLY61, LYS62, THR63, TY101, GLN125, MET128, ARG163, ARG176, and ARG222 involved in hydrogen bond formation and had the shortest distance of 1.9 Å with THR63, and ILE100, MET128, ALA168, TYR172, ARG176, ARG220, and ARG222 were making hydrophobic interactions (Table 9). FCA was found to make two hydrogen bonds GLN125 and ARG163 and three hydrophobic bonds with MET128, ALA168, and TYR172. Van der Waals interactions were also observed with TRP88, ILE100, TYR132, ALA167, and MET231 (Table 9). SARS-CoV-2 helicase (7NNG) had binding energy ranging from − 3.6 to − 6 kcal/mol (Table 3) with residues PRO284, GLY285, THR286, GLY287, LYS288, GLN404, GLY538, and ARG567 involved in hydrogen bond formation and had the shortest distance of 1.8 Å with GLY287, and only LYS288 and ARG443 were found to be involved in hydrophobic interactions (Table 9). HSV type 1 DNA polymerase (2GV9) binding energy ranged from − 3.5 to − 4.6 kcal/mol (Table 3) with residues PHE718, LEU721, ASN815, and ASP888 involved in hydrogen bond formation with the shortest distance of 2 Å with LEU721, and only PRO723 was found to be involved in hydrophobic interaction (Table 9). Hepatitis B virus core protein (5GMZ) had a range of − 3.6 to − 4.8 kcal/mol of binding energy (Table 3) with residues ILE139 and LEU140 forming hydrogen bonds; only LEU143 involved in hydrophobic interactions, (Table 9), and THR114, GLU117, TYR118, SER121, PRO138, THR142 were involved in van der Waals interactions. Hepatitis C virus NS3-4A protease-helicase (4A92) had a range of − 3.8 to − 5.6 kcal/mol of binding energy (Table 3) with residues SER42, HIS57, GLY58, LEU135, GLY137, and SER139 forming hydrogen bonds and only LYS136 found to be involved in hydrophobic interactions (Table 9). SARS-CoV main protease (2GZ7) had a range of − 3.6 to − 5 kcal/mol binding energy (Table 3) with residues LEU141, ASN142, GLY143, and SER144 forming hydrogen bonds, and only CYS145 was involved in hydrophobic interactions (Table 9). HIV protease (6P9A) had a range of − 3.7 to − 4.9 kcal/mol of binding energy (Table 3) by mainly forming van der Waals interactions with residues GLN270, HIS278, PHE292, THR296, VAL297, and SER298, and only ASP293, VAL280, and LYS291 involved in hydrogen bond formation and hydrophobic interactions respectively (Table 9). COVID-19 main protease (6LU7) had a range of − 3.8 to − 5.2 kcal/mol of binding energy (Table 3) with

Table 9 Antiviral target protein's residues involved in docking and interaction with ligand (hydrogen bond, hydrophobic, and electrostatic interactions)

Ligand	PDB ID	ΔG_b (binding energy), kcal/mol	Hydrogen bonds		Hydrophobic and electrostatic interactions		
			Interacting residues	Distance	Type	Interacting residues	Distance
	2KI5	−5.2	MET60 GLY61 LYS62 LYS62 ARG222	2.16709 2.15534 2.14363 3.25049 2.45797	Pi-cation Pi-alkyl	ARG222 ARG220	3.61979 4.70778
HMF	7NNG	−5.1	GLY285 LYS288 GLN404 GLY538 ARG567 PRO284	2.54675 2.12474 2.64366 2.41493 1.98665 3.62445	Pi-cation Pi-cation	LYS288 ARG443	3.44219 3.48096
BHMF	2KI5	−5.2	GLY61 LYS62 THR63 ARG222	2.08313 2.16206 1.99345 2.406	Pi-cation Pi-alkyl	ARG222 ARG220	3.59202 4.7977
EL	2KI5	−5.4	TY101 GLN125 ARG176	2.0784 2.20069 2.26532	Alkyl Alkyl Pi-alkyl Pi-alkyl	ILE97 ARG222 HIS58 TYR101	3.81674 3.90927 5.18368 4.95048
EMF	2KI5	−5.7	ARG163 GLN125	2.73403 3.53644	Pi-sigma Pi-pi stacked Alkyl Alkyl Pi-alkyl Pi-alkyl	MET128 TYR172 ILE100 ARG176 TYR172 ALA168	3.71617 4.02036 4.17508 4.61953 4.79532 4.63072
FCA	2KI5	−6	GLN125 ARG163 MET128	2.3539 2.85578 3.52861	Pi-sigma Pi-pi stacked Pi-alkyl	MET128 TYR172 ALA168	3.52861 3.891 5.23958
	4A92	−5.6	HIS57 HIS57 SER139 SER139 SER139 LEU135 SER42 GLY58 HIS57 GLY137	2.43641 2.82716 2.1591 2.47954 2.48106 1.85607 2.24743 3.56748 3.12733 2.6931	Pi-alkyl	LYS136	5.38216
	2GZ7	−5	LEU141 ASN142 GLY143 SER144	2.67596 3.12851 2.85492 2.12648	Pi-sulfur	CYS145	5.00373
	6LU7	−5.2	GLY143 CYS145 LEU141	2.08654 2.39242 2.16295	Pi-alkyl	CYS145	5.43919
	7NNG	−6	GLY285 THR286 GLY287 LYS288 GLN404 GLY538 ARG567 PRO284	2.59245 2.61741 1.89529 2.80725 2.62826 2.45127 2.0057 3.74558	Pi-cation Pi-cation	LYS288 ARG443	3.45639 3.58821

Table 9 (continued)

Ligand	PDB ID	ΔG_b (binding energy), kcal/mol	Hydrogen bonds		Hydrophobic and electrostatic interactions		
			Interacting residues	Distance	Type	Interacting residues	Distance
FDC	7NNG	−5	GLY285	2.59245	Pi-cation	LYS288	3.45639
			THR286	2.61741	Pi-cation	ARG443	3.58821
			GLY287	1.89529			
			LYS288	2.80725			
			GLN404	2.62826			
			GLY538	2.45127			
			ARG567	2.0057			
			PRO284	3.74558			

residues GLY143, CYS145, and LEU141 forming hydrogen bonds and only CYS145 was taking part in hydrophobic interactions (Table 9).

Molecular Dynamic Simulation

MD simulations under physiological conditions were run to examine the stability of the protein–ligand docked complex with the most favorable interactions and the binding pose generated by docking. The values were derived after performing independent runs of 100 ns in the MD simulations of the protein–ligand complexes and proteins. We were able to determine the stability of the docked complexes using the root mean square deviation (RMSD) of each trajectory in relation to its initial conformation as acquired from MD simulations with other parameters. During the simulation process, RMSD is a crucial metric to analyze the equilibration of MD trajectories and verify the stability of complex systems [26]. The atomic RMSDs of the backbone for the protein and the ligand were calculated and plotted in a time-dependent manner. When analyzing the stability and flexibility of complex systems through simulation, RMSF is yet another significant parameter. The behavior of the target protein's amino acid residues when they bind to a ligand was analyzed using RMSF [27]. Similarly, the complex systems' radius of gyration (Rg) was examined. Rg is the protein atoms' root mean square distance from the axis of orientation [28]. It is one of the crucial metrics that capture how the protein structure's size and overall compactness vary throughout the simulation [29]. Proteins with higher Rg values are more flexible and less compact, whereas those with lower values are stiffer and more compact [27]. All complexes underwent solvent accessible surface area (SASA) analysis, for the purpose of determining the degree of receptor exposure to the surrounding solvent molecules during simulation. SASA is an important metric. In general, ligand binding can alter the receptor structurally, changing the area that comes into touch with the solvent [30].

LasR Ligand-Binding Domain (2UVO)

Figure 5 shows the RMSD, SASA, RMSF, and Rg of 100-ns trajectories for the simulated ligand-bound and unbound system. The RMSD trajectory showed a movement between 0.16716 and 0.454912 nm with an average of 0.387007 nm and 0.17068 and 0.41594 nm with an average of 0.359497 nm for bound and unbound protein respectively (Fig. 5). At the beginning (up to 10 ns), there was a rise in RMSD which started to stabilize thereafter

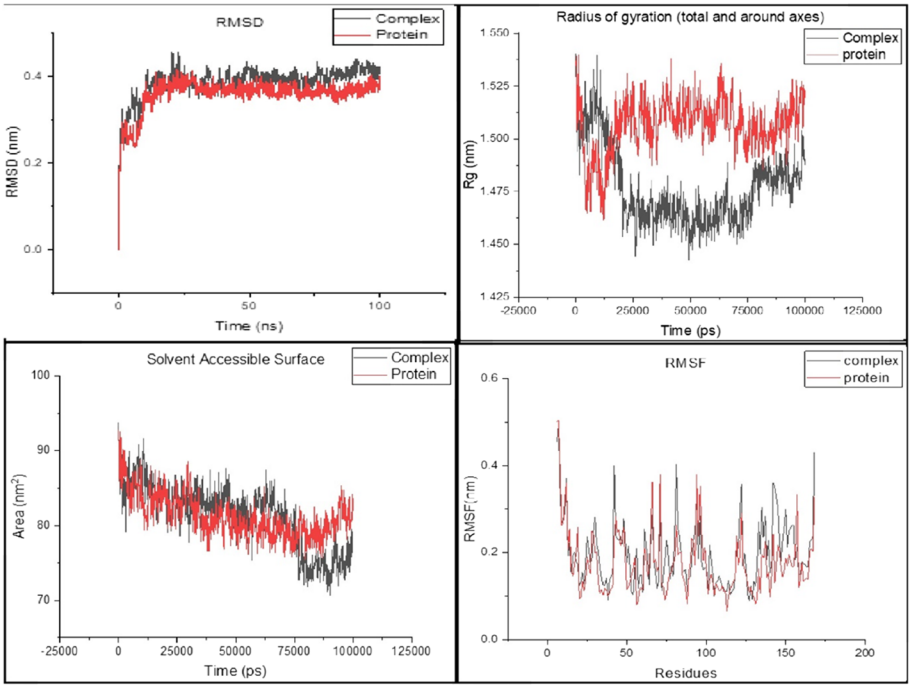

Fig. 5 LasR (2UVO) and FCA complex MD simulation trajectories comprising root mean square deviation (RMSD), radius of gyration (Rg), solvent accessible surface area (SASA), and root mean square fluctuations (RMSF)

and remained between 0.35 and 0.45 nm and 0.34 and 0.41 nm for bound and unbound protein respectively. Towards the end, RMSD further stabilized after 80 ns and remained between 0.38 and 0.44 nm with an average of 0.410401 nm for the ligand-bound protein. The RMSD values for ligand fluctuated in the beginning and remained between 0.34817 and 1.193063 nm with an average value of 0.893418 nm throughout the observation. The ligand RMSD stabilized after 15 to 18 ns and remained stabilized till 90 ns with values between 0.7514 and 1.0684 nm with an average of 0.923449 nm. The root mean square fluctuations (RMSF) of residues in the protein backbone remained in a range of 0.0877–0.4933 nm with an average of 0.198139 nm and 0.0649–0.5038 nm with an average of 0.176577 nm for bound and unbound protein respectively (Fig. 5). Except for some regions with sharp fluctuations, the rest of the regions seemed comparatively aligned with unbound protein residues. The radius of gyration (Rg) as a function of simulation time was estimated to be in the range of 1.44251–1.54047 nm with an average of 1.476528 nm and 0.146136–1.54007 nm with an average of 1.506529 nm for bound and unbound protein respectively (Fig. 5). The Rg value for the complex initially fluctuated, then dropped till 20 ns, then again stabilized, and remained between 1.44 and 1.48 nm with stability till 80 ns and then increased a little to be stabilized again. In contrast to this, the unbound protein had higher Rg values, fluctuated till 20 ns, then increased, and stabilized within 1.48–1.53 nm with an average of 1.50 nm. The solvent accessible surface area (SASA) fluctuated in the range of 70.611–93.737 nm^2 with an average of 81.22337 nm^2 and 75.457–92.825 nm^2 with an average of 81.23671 nm^2 for bound and unbound protein respectively (Fig. 5). In

addition, it was discovered how many hydrogen bonds there were between proteins and its ligand. It was discovered that the amount of hydrogen bonds between the receptor and ligand changed between 0 and 3.

Human Acetylcholinesterase (AChE) (4BDT)

Figure 6 shows the RMSD, SASA, Rg, and RMSF of 100-ns trajectories for the simulated ligand-bound and unbound system. The protein RMSD of 100-ns trajectories for the simulated system showed a movement between 0.146732 and 0.517783 nm with an average of 0.423525 and 0.162652 and 0.8154783 nm with an average of 0.729546 nm for bound and unbound protein respectively (Fig. 6). The ligand-bound protein RMSD further stabilized after 35 ns and fluctuates within a range of 0.401907–0.517783 nm with an average of 0.475935 nm. The unbound protein RMSD achieved equilibrium after around 20 ns. The RMSD values for ligand fluctuated in the range of 0.169745–1.209972 nm with an average of 0.635599. The ligand RMSD remained stable till 75 ns with a range of 0.403872–0.66521 nm with an average of 0.513038, and then follows a sharp rise and stabilized again (Fig. 6). The root mean square fluctuations (RMSF) of residues in the protein backbone remained in a range of 0.0615–1.0026 nm with an average of 0.195687 nm and 0.0752–1.2521 nm with an average of 0.204796 nm for bound and unbound protein respectively (Fig. 6). The radius of gyration (Rg) as a function of simulation time was estimated to be in the range of 2.4106–2.56557 nm with an average value of 2.524177 nm and 2.28115–2.53649 nm with an average of 2.326197 nm for bound and unbound protein respectively (Fig. 6). Rg values for ligand-bound protein rose from 35 to 40 ns and then again stabilized within the range of 2.53025–2.56557 nm with an average value of 2.547155 nm. The solvent accessible surface area (SASA) fluctuated in a range of 201.035–244.34 nm^2 with an average of 216.7433 nm^2 and 195.352–245.408 nm^2 with an average of 211.236 nm^2 for bound and unbound protein respectively (Fig. 6). Furthermore, the number of hydrogen bonds between proteins and ligands was determined. It was found that the number of hydrogen bonds between receptor and ligand fluctuated between 0 and 3.

S. aureus Tyrosyl-tRNA Synthetase (1JIJ)

The MD simulation trajectories of tyrosyl-tRNA synthetase (1JIJ) (Fig. 7) were analyzed for RMSD, SASA, Rg, and RSMF of unbound protein and ligand-bound protein complex. RMSD trajectory showed a rather stable pattern; the RMSD values ranged from 0.17179 to 0.44238 nm with an average of 0.35337 nm and 0.18562 to 0.48957 nm with an average of 0.41549 nm for bound and unbound protein respectively. The ligand-bound protein achieves equilibrium almost instantaneously, while unbound protein takes about 20 ns to attain equilibrium. The ligand-bound protein also showed some rapid fluctuation around 65–75 ns and attained the same values as of unbound protein. The SASA trajectories had a range of 133.99–166.632 nm^2 with an average of 148.687 nm^2 and 129.298–168.684 nm^2 with an average of 140.323 nm^2 for bound and unbound protein respectively. The values of bound and unbound protein remained similar for 20 ns and then diverged to converge again at 80 ns. During 20–80 ns, the SASA values had a range of 138.633–162.336 nm^2 with an average of 149.3857 nm^2 and 129.298–147.578 nm^2 with an average of 137.446 nm^2 for bound and unbound protein respectively. The radius of gyration (Rg) values ranged

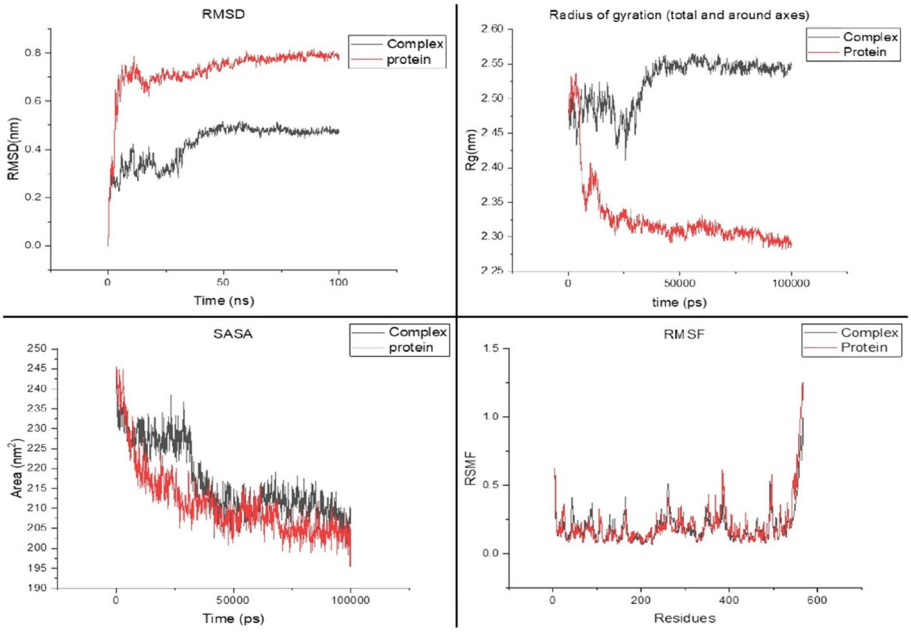

Fig. 6 Human acetylcholinesterase (AChE) (4BDT) and FCA complex MD simulation trajectories comprising root mean square deviation (RMSD), radius of gyration (Rg), solvent accessible surface area (SASA), and root mean square fluctuations (RMSF)

from 1.95592 to 2.1715 nm with an average of 2.02531 nm and 1.91111 to 2.07657 nm with an average of 1.94831 nm for bound and unbound protein respectively. Rg for ligand-bound protein was found to be higher than unbound protein Rg stabilized earlier for unbound protein, whereas Rg values for ligand-bound protein remained declining for the first 50 ns and then stabilized. Rg values for 50–100 ns remained stabilized in a range of 1.95592–2.0484 nm with an average of 1.99114 nm and 1.91489–1.97051 nm with an average of 1.93687 nm for bound and unbound protein respectively. The RMSF remained in a range of 0.0756–0.6391 nm with an average of 0.21014 nm and 0.0718–0.6848 nm with an average of 0.18632 nm for bound and unbound protein respectively. The RMSF of the protein remained almost the same and almost similar even after the ligand bound to the active site, except for a few regions where fluctuations are quite observable (residues 148–162 and 235–247). Furthermore, the hydrogen bonds between ligand and protein ranged from 0 to 3 which is in contrast to docking mode where about 5 to 6 hydrogen bonds are observed; this indicated most of the hydrogen bonds do not sustain during simulation.

Discussion

The most frequent cause of senile dementia, AD, is a serious public health concern with negative effects on both the economy and people. Although other treatment plans have been suggested [31, 32], the majority of available therapy methods focus on raising the brain's acetylcholine levels. Current licensed anti-AD medications include donepezil, rivastigmine, and galanthamine, which are AChE (human AChE [acetylcholinesterase])

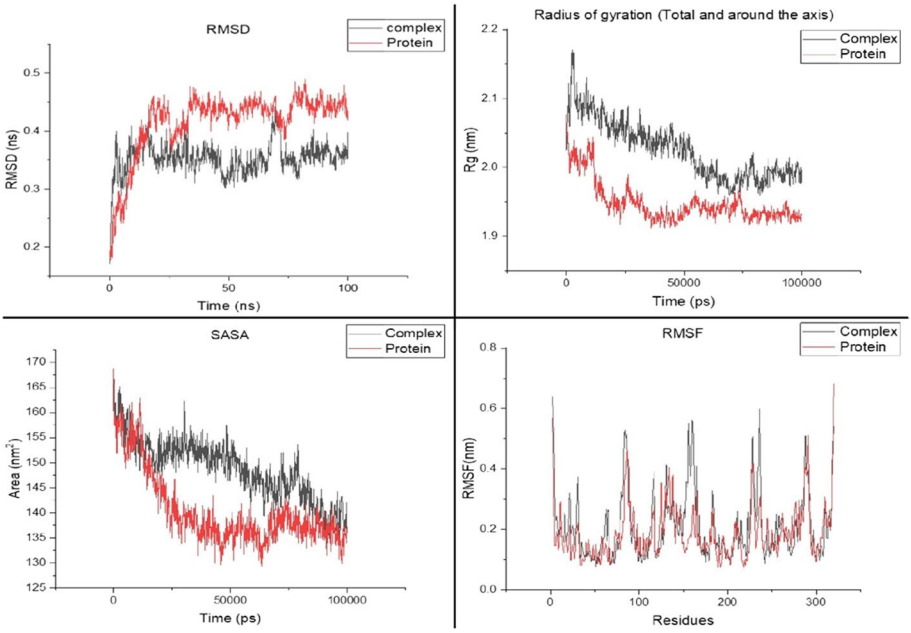

Fig. 7 Tyrosyl-tRNA synthetase (1JIJ) and FCA complex MD simulation trajectories comprising root mean square deviation (RMSD), radius of gyration (Rg), solvent accessible surface area (SASA), and root mean square fluctuations (RMSF)

inhibitors [33]. The discovery of MTDLs (multitarget-directed ligands), which act simultaneously on various elements of AD pathogenesis, was inspired by the complicated etiology of AD [34].

We found that our compounds of interest primarily interacted with butyrylcholinesterase (BuChE) (4BDS) and acetylcholinesterase (AChE) (4BDT). By examining FCA's network of interactions, we saw its binding and interactions with various important residues in the BuChE active site, most notably SER198 in van der Waals interactions, which is part of the catalytic triad. It also forms hydrogen bonds with the oxyanion hole residues GLY116 and GLY117, as well as hydrophobic contacts with the highly conserved anionic site residue TRP82 [35]. HMF and EMF also formed hydrogen bonds with GLY116 and GLY117, as well as hydrophobic contacts with TRP82 and one of the catalytic triad residues, HIS438, respectively. These interactions make them appropriate BuChE inhibitors and enhance their therapeutic potential. FCA was also a good fit for AChE's active site. TRP86 and HIS447 are key active site residues that play an important role in the orientation of the acetylcholine molecules that enter the active site. TRP86 and HIS447 residues bind together to position the charged side of acetylcholine in the active site of the native enzyme, facilitating its interaction with SER203 [36, 37]. These results are consistent with other studies with these enzymes [38, 39] and made FCA, HMF, and EMF potent compounds with dual affinity.

To comprehend the compound's binding mechanism, structural behavior, and flexibility, we conducted 100 ns of MD simulations for the AChE (4BDT)-ligand complex and protein. The unbound protein reached equilibrium after 25 ns (Fig. 5) and the ligand-bound protein complex remained stable after 30 ns, with the most stable period lasting from 30 to 75 ns (Fig. 5). The analysis of the RMSF plots revealed that the significantly fluctuating

regions containing amino acids are located at the protein's N-terminus (up to the first 10 amino acids) and C-terminus (557–567 amino acids). The protein's N-terminal region is highly mobile, with an average value of 0.23 nm. Furthermore, the C-terminal region of the protein, particularly amino acids 545–567, had increased mobility (0.5 nm) than other regions of the protein, which decreased after the ligand was bound to the active site (Fig. 5). The analysis suggests a change in protein flexibility after ligand binding. Whereas the protein's solvent accessible surface area (SASA) (Fig. 5) indicates the overall SASA of the protein, the complex displayed decreased SASA after 30 ns of simulation, indicating the reduction in the protein's structural compactness. In contrast, the radius of the gyration study (Fig. 5) revealed that the complex exhibited a greater radius of gyration, indicating loose packing of the protein structure after 30 ns, which ultimately corroborated the SASA results.β-Lactamases (BLs) are one of the most frequent causes of bacterial resistance to β-lactam antibiotics, especially in Gram-negative bacteria [40]. Extended-spectrum spectral cephalosporin-resistant Gram-negative bacteria are a common source of the class C enzymes, also known as AmpC-type β-lactamases [41]. The active site pocket of class C β-lactamases has four conserved structural motifs with class A β-lactamases, including Ser64-X-X-Lys67, Tyr150-X-Asn152, Lys315-Thr316-Gly317, and the Ω-loop [42]. When docked with AmpC-type β-lactamases (1FR6), FCA was shown to have the most favorable binding energy, followed by EMF, BHMF, and HMF (Table 3). FCA interacted with conserved structural motifs in the active site (SER64, GLU272, LYS315, SER318, ASN346, GLY317, TYR150, ALA298, ARG148, LEU293, THR316, and GLY317) (Table 5). FCA was found to engage all probable critical active site residues and may be a good inhibitor of AmpC-type β-lactamases (Fig. 2).

Quorum sensing (QS), a cell density-dependent bacterial communication system, is known to be used by many pathogenic microbes to regulate a variety of virulence traits, adding to its pathogenicity. LasI/LasR and RhlI/RhlR are the two main interconnected circuits that make up the QS system. In the current work, we examined a number of significant QS pathway targets from various microorganisms. We found that every molecule of interest interacted with the target receptors in great detail. Rajkumari et al. (2019) had similar results with HMF's strong interaction with *P. aeruginosa* LasR (2UV0) protein and inhibition of bacterial biofilm formation [43]. Additionally, we found that FCA was perfectly suited to the LasR active site. When FCA docked with LasR, the several active site residues (TYR56, TYR64, TYR93, LEU110, SER129, ALA105, LEU110, ASP73, LEU36, TRP60, THR75, VAL76, TRP88, ILE92, and PHE101) (Table 7) were found to be interacting with the ligand. Rajkumari et al. (2019) noted that the crucial active site residues were TYR56, ASP73, and SER129, all of which were bound to the FCA (Fig. 3). Additional investigation using MD simulation showed that the RMSD values of the complex remained nearly equal to the RMSD of protein alone, with average values of 0.387 and 0.359, respectively. During the simulation process, RMSD is a crucial measure to examine the equilibration of MD trajectories and verify the stability of complex systems. With the ligand's binding, the Rg of the protein–ligand complex decreased, adding to its stability. The protein and protein complex's SASA behaved similarly, remaining essentially constant and stable. All of these findings strongly imply that FCA is a potential QS pathway inhibitor with HMF and EMF having potential in them.

Aminoacyl-tRNA synthetases (specifically, tyrosyl-tRNA synthetases) (1JIJ) are essential for protein synthesis because they generate charged tRNAs. Because of the relevance of the synthetases, drugs that selectively block bacterial aminoacyl-tRNA synthetases can be made into potent antibacterial pharmaceuticals. In our study, we

observed that our compounds of interest, such as HMF, EMF, FCA, and FDC, interact favorably with *S. aureus* tyrosyl-tRNA synthetase (1JIJ). When docked with tyrosyl-tRNA synthetase, FCA had the best binding energy (−6.7 kcal/mol) and interacted with several active site residues (CYS37, GLY38, THR75, TYR170, GLN174, GLN190, LEU70, TYR36, ALA39, ASP40, ASN124, ASP177, GLN196, and ILE200) (Table 8). These all residues are part of the α/β domain of the protein which has a six-stranded parallel β-sheet and a deep active site cleft that binds ligands such as tyrosine found in this protein. The tyrosine amino group forms hydrogen bonds with TYR170 and GLN174, and the phenolic hydroxyl group forms hydrogen bonds with ASP177 and TYR36 [44–46]. The MD simulation study of tyrosyl-tRNA synthetases with FCA in its active site and tyrosyl-tRNA synthetases alone in water revealed this complex's stability and viability. The RMSD of the protein decreased after ligand (FCA) binds at the active site and this complex achieves equilibrium even before the protein. The RMSD and RMSF findings demonstrated that binding of the ligands had no significant influence on the protein's flexibility. Where else the Rg values increased after binding of ligand and SASA of the protein decreased after binding of ligand to the active site suggests that the simulation minimized the surface area of proteins in complexes.

Most antiviral medications work by primarily inhibiting HSV-1 thymidine kinase (TK), phosphorylating it, and then using DNA polymerase to stop DNA elongation. Acyclovir, famciclovir, and valacyclovir are examples of nucleoside analogs used in standard therapy to combat viral DNA polymerase [47]. However, their continued use in immunocompromised patients may lead to episodes of treatment failures, ultimately leading to the emergence of viral strains that are resistant to antivirals [47]. There is a need for new potent inhibitory compounds. In the current study, we found EMF and FCA had some potential. FCA was found to make interactions with residues GLN125, ARG163, MET128, ALA168, TYR172, TRP88, ILE100, TYR132, ALA167, and MET231. All these residues are part of the HSV 1 TK (2KI5) active site, and this mimics the location and interactions of the 5′-hydroxyl of substrate dT [48–50].

The SARS-CoV-2 virus, which is at the base of the global COVID-19 outbreak, is now untreatable. The SARS-CoV-2 non-structural protein 13 (NSP13), with its great sequence conservation and crucial function in viral replication, has been identified as a target for antivirals. Two "druggable" pockets on NSP13 are among the most conserved areas in the entire SARS-CoV-2 proteome, according to structural analyses. Here, we tried to observe the interaction of our compound of interest with the SARS-CoV-2 helicase (7NNG). Only HMF and FCA have shown some potential. The HMF and FCA both bind to the ATP binding site residues in helicase's conserved domain [51].

Conclusion

The therapeutic profile of HMF and its derivatives were investigated. Our compounds interacted most efficiently with anti-quorum sensing targets, followed by Alzheimer's and antimicrobial targets. Some of the best targets of HMF and its derivatives were found to be transcription factors Trar (1H0M) and LasR (2UV0), human butyrylcholinesterase (4BDS), human acetylcholinesterase (4BDT), tyrosyl-tRNA synthetase (1JIJ), and dihydrofolate reductase. Furthermore, beta-lactamase (1FR6) and SARS-CoV-2 helicase (7NNG) interacted well with them. All seven compounds had some potential in the target fields, but FCA fared the best, followed by EMF and HMF.

Author Contribution S. K. Singh—conducted the experiments, data validation, and writing of the draft of the manuscript.

Y. Kumar—conceptualization of the experiments, data analysis, supervision.

S. Sasmal—data analysis, supervision.

All the authors read and approve the final manuscript.

Funding This work was supported by Netaji Subhas University of Technology, New Delhi, India.

Data Availability Not applicable.

Declarations

Ethical Approval Not applicable.

Consent to Participate Not applicable.

Consent for Publication Not applicable.

Conflict of Interest The authors declare no competing interests.

References

1. van Putten, R. J., van der Waal, J. C., de Jong, E., et al. (2013). Hydroxymethylfurfural, a versatile platform chemical made from renewable resources. *Chemical Reviews, 113*, 1499–1597. https://doi.org/10.1021/CR300182K/ASSET/IMAGES/CR300182K.SOCIAL.JPEG_V03
2. Aresta M, Dibenedetto A (2019) Beyond fractionation in the utilization of microalgal components. Bioenergy with carbon capture and storage: Using natural resources for sustainable development 173–193 https://doi.org/10.1016/B978-0-12-816229-3.00009-0
3. Hou, Y. C., Ching, H., Chao, P. D. L., et al. (2005). Effects of glucose, fructose and 5-hydroxymethyl-2-furaldehyde on the presystemic metabolism and absorption of glycyrrhizin in rabbits. *Journal of Pharmacy and Pharmacology, 57*, 247–251. https://doi.org/10.1211/0022357055281
4. Morone, A., Apte, M., & Pandey, R. A. (2015). Levulinic acid production from renewable waste resources: Bottlenecks, potential remedies, advancements and applications. *Renewable and Sustainable Energy Reviews, 51*, 548–565. https://doi.org/10.1016/j.rser.2015.06.032
5. Neves, P., Lima, S., Pillinger, M., et al. (2013). Conversion of furfuryl alcohol to ethyl levulinate using porous aluminosilicate acid catalysts. *Catalysis Today, 218–219*, 76–84. https://doi.org/10.1016/J.CATTOD.2013.04.035
6. van Nguyen, C., Lewis, D., Chen, W. H., et al. (2016). Combined treatments for producing 5-hydroxymethylfurfural (HMF) from lignocellulosic biomass. *Catalysis Today, 278*, 344–349. https://doi.org/10.1016/J.CATTOD.2016.03.022
7. Hou, Q., Qi, X., Zhen, M., et al. (2021). Biorefinery roadmap based on catalytic production and upgrading 5-hydroxymethylfurfural. *Green Chemistry, 23*, 119–231. https://doi.org/10.1039/D0GC02770G
8. Chen, G., Wu, L., Fan, H., & Li, B. G. (2018). Highly efficient two-step synthesis of 2,5-furandicarboxylic acid from fructose without 5-hydroxymethylfurfural (hmf) separation: In situ oxidation of hmf in alkaline aqueous H2O/DMSO mixed solvent under mild conditions. *Industrial and Engineering Chemistry Research, 57*, 16172–16181. https://doi.org/10.1021/ACS.IECR.8B03589/SUPPL_FILE/IE8B03589_SI_001.PDF
9. CN110575450 Application of 2,5-furan dimethanol in preparing antitumor drugs. https://patentscope.wipo.int/search/en/detail.jsf?docId=CN279820154&docAn=201910876855.3. Accessed 4 Oct 2022
10. Yan, T., Feringa, B. L., & Barta, K. (2016). Benzylamines via iron-catalyzed direct amination of benzyl alcohols. *ACS Catalysis, 6*, 381–388. https://doi.org/10.1021/ACSCATAL.5B02160/SUPPL_FILE/CS5B02160_SI_001.PDF
11. Yan, L., Zhang, Q., Deng, W., et al. (2020). Catalytic valorization of biomass and bioplatforms to chemicals through deoxygenation. *Advances in Catalysis, 66*, 1–108. https://doi.org/10.1016/BS.ACAT.2020.09.002

12. 2,5-dimethylfuran (CHEBI:89052). https://www.ebi.ac.uk/chebi/searchId.do?chebiId=CHEBI:89052. Accessed 4 Oct 2022
13. Ventura, M., Dibenedetto, A., & Aresta, M. (2018). Heterogeneous catalysts for the selective aerobic oxidation of 5-hydroxymethylfurfural to added value products in water. *Inorganica Chim Acta, 470*, 11–21. https://doi.org/10.1016/J.ICA.2017.06.074
14. Cragg, G. M., & Newman, D. J. (2013). Natural products: A continuing source of novel drug leads. *Biochimica et Biophysica Acta (BBA) General Subjects, 1830*, 3670–3695. https://doi.org/10.1016/J.BBAGEN.2013.02.008
15. Bajorath, J. (2002). Integration of virtual and high-throughput screening. *Nature Reviews Drug Discovery, 1*(11), 882–894. https://doi.org/10.1038/nrd941
16. Pires, D. E. V., Blundell, T. L., & Ascher, D. B. (2015). pkCSM: Predicting small-molecule pharmacokinetic and toxicity properties using graph-based signatures. *Journal of Medicinal Chemistry, 58*, 4066–4072. https://doi.org/10.1021/ACS.JMEDCHEM.5B00104/SUPPL_FILE/JM5B00104_SI_001.PDF
17. Eberhardt, J., Santos-Martins, D., Tillack, A. F., & Forli, S. (2021). AutoDock Vina 1.2.0: New docking methods, expanded force field, and python bindings. *Journal of Chemical Information and Modeling, 61*, 3891–3898. https://doi.org/10.1021/ACS.JCIM.1C00203/SUPPL_FILE/CI1C00203_SI_002.ZIP
18. Berendsen, H. J. C., van der Spoel, D., & van Drunen, R. (1995). GROMACS: A message-passing parallel molecular dynamics implementation. *Computer Physics Communications, 91*, 43–56. https://doi.org/10.1016/0010-4655(95)00042-E
19. Lindahl, E., Hess, B., & van der Spoel, D. (2001). GROMACS 3.0: A package for molecular simulation and trajectory analysis. *Molecular modeling annual, 7*(8), 306–317. https://doi.org/10.1007/S008940100045
20. van der Spoel, D., Lindahl, E., Hess, B., et al. (2005). GROMACS: Fast, flexible, and free. *Journal of Computational Chemistry, 26*, 1701–1718. https://doi.org/10.1002/JCC.20291
21. van Aalten, D. M. F., Bywater, R., Findlay, J. B. C., et al. (1996). PRODRG, a program for generating molecular topologies and unique molecular descriptors from coordinates of small molecules. *Journal of Computer-Aided Molecular Design, 10*(3), 255–262. https://doi.org/10.1007/BF00355047
22. Ventola CL (2015) The antibiotic resistance crisis: Part 1: Causes and threats. Pharmacy and Therapeutics 40:277
23. Ben-Ami, R., & Kontoyiannis, D. P. (2021). Resistance to antifungal drugs. *Infectious Disease Clinics of North America, 35*, 279–311. https://doi.org/10.1016/J.IDC.2021.03.003
24. Ruma YN, Keniya M v., Tyndall JDA, Monk BC (2022) Characterisation of Candida parapsilosis CYP51 as a drug target using Saccharomyces cerevisiae as host. Journal of Fungi Vol 8 69 8 69 https://doi.org/10.3390/JOF8010069
25. Kawsar SMA, Almalki FA, Hadd T ben, et al (2022) Potential antifungal activity of novel carbohydrate derivatives validated by POM, molecular docking and molecular dynamic simulations analyses 1–16 https://doi.org/10.1080/08927022.2022.2123948
26. Kalimuthu, A. K., Panneerselvam, T., Pavadai, P., et al. (2021). Pharmacoinformatics-based investigation of bioactive compounds of Rasam (South Indian recipe) against human cancer. *Scientific Reports, 11*(1), 1–19. https://doi.org/10.1038/s41598-021-01008-9
27. Kumar B, Parasuraman P, Murthy TPK, et al (2022) In silico screening of therapeutic potentials from Strychnosnux-vomica against the dimeric main protease (Mpro) structure of SARS-CoV-2. J Biomol Struct Dyn 40 https://doi.org/10.1080/07391102.2021.1902394
28. Rahman, M. M., Saha, T., Islam, K. J., et al. (2021). Virtual screening, molecular dynamics and structure-activity relationship studies to identify potent approved drugs for Covid-19 treatment. *Journal of Biomolecular Structure & Dynamics, 39*, 1–11. https://doi.org/10.1080/07391102.2020.1794974
29. Gupta, S., Singh, A. K., Kushwaha, P. P., et al. (2021). Identification of potential natural inhibitors of SARS-CoV2 main protease by molecular docking and simulation studies. *Journal of Biomolecular Structure & Dynamics, 39*, 4334–4345. https://doi.org/10.1080/07391102.2020.1776157
30. Ghosh, S. K., Saha, B., & Banerjee, R. (2021). Insight into the sequence-structure relationship of TLR cytoplasm's Toll/Interleukin-1 receptor domain towards understanding the conserved functionality of TLR 2 heterodimer in mammals. *Journal of Biomolecular Structure & Dynamics, 39*, 1–10. https://doi.org/10.1080/07391102.2020.1786457
31. Holzgrabe, U., Kapková, P., Alptüzün, V., et al. (2007). Targeting acetylcholinesterase to treat neurodegeneration. *Expert Opinion on Therapeutic Targets, 11*, 161–179. https://doi.org/10.1517/14728222.11.2.161
32. Castro, A., Conde, S., Rodriguez-Franco, M., & Martinez, A. (2002). Non-cholinergic pharmacotherapy approaches to the future treatment of Alzheimer's disease. *Mini Reviews in Medicinal Chemistry., 2*, 37–50. https://doi.org/10.2174/1389557023406610

33. Smith, D. A. (2009). Treatment of Alzheimer's disease in the long-term-care setting. *American Journal of Health System Pharmacy, 66*, 899–907. https://doi.org/10.2146/AJHP070622
34. León, R., Garcia, A. G., & Marco-Contelles, J. (2013). Recent advances in the multitarget-directed ligands approach for the treatment of Alzheimer's disease. *Medicinal Research Reviews, 33*, 139–189. https://doi.org/10.1002/MED.20248
35. Bajda, M., Więckowska, A., Hebda, M., et al. (2013). Structure-based search for new inhibitors of cholinesterases. *International Journal of Molecular Sciences, 14*, 5608–5632. https://doi.org/10.3390/IJMS14035608
36. Dvir, H., Silman, I., Harel, M., et al. (2010). Acetylcholinesterase: From 3D structure to function. *Chemico-Biological Interactions, 187*, 10–22. https://doi.org/10.1016/J.CBI.2010.01.042
37. Johnson, J. L., Cusack, B., Hughes, T. F., et al. (2003). Inhibitors tethered near the acetylcholinesterase active site serve as molecular rulers of the peripheral and acylation sites. *Journal of Biological Chemistry, 278*, 38948–38955. https://doi.org/10.1074/jbc.M304797200
38. Yusufzai SK, Khan MS, Sulaiman O, et al (2018) Molecular docking studies of coumarin hybrids as potential acetylcholinesterase, butyrylcholinesterase, monoamine oxidase A/B and β-amyloid inhibitors for Alzheimer's disease. Chemistry Central Journal 12 1 12 1–57 https://doi.org/10.1186/S13065-018-0497-Z
39. Mascarenhas, A. M. S., de Almeida, R. B. M., de Araujo Neto, M. F., et al. (2021). Pharmacophore-based virtual screening and molecular docking to identify promising dual inhibitors of human acetylcholinesterase and butyrylcholinesterase. *Journal of Biomolecular Structure & Dynamics, 39*, 6021–6030. https://doi.org/10.1080/07391102.2020.1796791
40. Sandanayaka, V., & Prashad, A. (2012). Resistance to β-lactam antibiotics: Structure and mechanism based design of & #946;-Lactamase Inhibitors. *Current Medicinal Chemistry, 9*, 1145–1165. https://doi.org/10.2174/0929867023370031
41. Palzkill, T. (2013). Metallo-β-lactamase structure and function. *Annals of the New York Academy of Sciences, 1277*, 91–104. https://doi.org/10.1111/J.1749-6632.2012.06796.X
42. Jacoby, G. A. (2009). AmpC B-lactamases. *Clinical Microbiology Reviews, 22*, 161–182. https://doi.org/10.1128/CMR.00036-08/ASSET/AE35DFAC-E4DF-4BE0-A0CB-2F00DE32723E/ASSETS/GRAPHIC/ZCM0010922700004.JPEG
43. Rajkumari, J., Borkotoky, S., Reddy, D., et al. (2019). Anti-quorum sensing and anti-biofilm activity of 5-hydroxymethylfurfural against Pseudomonas aeruginosa PAO1: Insights from in vitro, in vivo and in silico studies. *Microbiological Research, 226*, 19–26. https://doi.org/10.1016/j.micres.2019.05.001
44. Qiu, X., Janson, C. A., Smith, W. W., et al. (2001). Crystal structure of Staphylococcus aureus tyrosyl-tRNA synthetase in complex with a class of potent and specific inhibitors. *Protein Science, 10*, 2008–2016. https://doi.org/10.1110/PS.18001
45. Matejić, J. S., Stojanović-Radić, Z. Z., Ristić, M. S., et al. (2018). Chemical characterization, in vitro biological activity of essential oils and extracts of three Eryngium L. species and molecular docking of selected major compounds. *Journal of Food Science and Technology, 55*, 2910–2925. https://doi.org/10.1007/S13197-018-3209-8/FIGURES/2
46. Nachiappan, M., Jain, V., Sharma, A., et al. (2020). Conformational changes in glutaminyl-tRNA synthetases upon binding of the substrates and analogs using molecular docking and molecular dynamics approaches. *Journal of Biomolecular Structure & Dynamics, 38*, 1575–1589. https://doi.org/10.1080/07391102.2019.1617787
47. Whitley, R. J. (2006). New approaches to the therapy of HSV infections. *Herpes, 13*, 53–55.
48. Bennett, M. S., Wien, F., Champness, J. N., et al. (1999). Structure to 1.9 A resolution of a complex with herpes simplex virus type-1 thymidine kinase of a novel, non-substrate inhibitor: X-ray crystallographic comparison with binding of aciclovir. *FEBS Letters, 443*, 121–125. https://doi.org/10.1016/S0014-5793(98)01619-6
49. SMA El-halim MA Mamdouh AE El-haddad SM Soliman (2020) Fabrication of anti-HSV-1 curcumin stabilized nanostructured proniosomal gel: Molecular docking studies on thymidine kinase proteins. Scientia Pharmaceutica, 2020 88 9 88 9 https://doi.org/10.3390/SCIPHARM88010009
50. Kant, K., Lal, U. R., Kumar, A., & Ghosh, M. (2019). A merged molecular docking, ADME-T and dynamics approaches towards the genus of Arisaema as herpes simplex virus type 1 and type 2 inhibitors. *Computational Biology and Chemistry, 78*, 217–226. https://doi.org/10.1016/J.COMPBIOLCHEM.2018.12.005

51. White MA, Lin W, Cheng X (2020) Discovery of COVID-19 inhibitors targeting the SARS-CoV-2 Nsp13 helicase. Journal of Physical Chemistry Letters 9144–9151. https://doi.org/10.1021/ACS.JPCLETT.0C02421/ASSET/IMAGES/LARGE/JZ0C02421_0005.JPEG